

Evolution and Distribution of Magnetic Fields from AGNs in Galaxy Clusters. I. The Effect of Injection Energy and Redshift

Hao Xu¹, Hui Li¹, David C. Collins², Shengtai Li¹, and Michael L. Norman²

ABSTRACT

We present a series of cosmological magnetohydrodynamic (MHD) simulations that simultaneously follow the formation of a galaxy cluster and evolution of magnetic fields ejected by an Active Galactic Nucleus (AGN). Specifically, we investigate the influence of both the epoch of AGN ($z \sim 3-0.5$) and the AGN energy ($\sim 3 \times 10^{57} - 2 \times 10^{60}$ ergs) on the final magnetic field distribution in a relatively massive cluster ($M_{vir} \sim 10^{15} M_{\odot}$). We find that as long as the AGN magnetic fields are ejected before the major mergers in the cluster formation history, magnetic fields can be transported throughout the cluster and can be further amplified by the intra-cluster medium (ICM) turbulence cause by hierarchical mergers during the cluster formation process. The total magnetic energy in the cluster can reach $\sim 10^{61}$ ergs, with micro Gauss fields distributed over \sim Mpc scale. The amplification of the total magnetic energy by the ICM turbulence can be significant, up to ~ 1000 times in some cases. Therefore even weak magnetic fields from AGNs can be used to magnetize the cluster to the observed level. The final magnetic energy in the ICM is determined by the ICM turbulent energy, with a weak dependence on the AGN injection energy. We discuss the properties of magnetic fields throughout the cluster and the synthetic Faraday rotation measure maps they produce. We also show that high spatial resolution over most of the magnetic regions of the cluster is very important to capture the small scale dynamo process and maintain the magnetic field structure in our simulations.

Subject headings: galaxies: active — galaxies: clusters: general — methods: numerical — MHD — turbulence

¹Theoretical Division, Los Alamos National Laboratory, Los Alamos, NM 87545; hao_xu@lanl.gov, hli@lanl.gov, sli@lanl.gov

²Center for Astrophysics and Space Sciences, University of California, San Diego, 9500 Gilman Drive, La Jolla, CA 92093; dcollins@physics.ucsd.edu, mlnorman@ucsd.edu

1. Introduction

There is growing evidence that the intracluster medium (ICM) of galaxy clusters is permeated with magnetic fields, as indicated by the detection of large-scale, diffused radio emission called radio halos and relics (e.g. Carilli & Taylor 2002; Ferrari et al. 2008; Giovannini et al. 2009). The radio halos are sometimes extended over ≥ 1 Mpc, covering the whole cluster. By assuming that the magnetic energy is comparable to the total energy in relativistic electrons, one often deduces that the magnetic fields in the cluster halos can reach $0.1 - 1.0 \mu\text{G}$ and the total magnetic energy can be as high as 10^{61} ergs (Feretti 1999).

The Faraday rotation measurements (FRM) are extensively used to study the magnetic fields in galaxy clusters. By combining FRM and density measurements, magnetic field strengths in clusters have been measured as high as a few to ten μG level, mostly in the cluster core region (Carilli & Taylor 2002). More interestingly, FRM was used to suggest that magnetic fields can have a Kolmogorov-like turbulent spectrum in the cores of clusters (Vogt & Enßlin 2003), with an energy spectrum peak at several kpc. Other studies (Eilek & Owen 2002; Taylor & Perley 1993; Colgate & Li 2000) have suggested that the coherence scales of magnetic fields can range from a few kpc to a few hundred kpc, implying large amounts of magnetic energy and fluxes in the ICM. Recently, radial profiles of magnetic fields extended to the outer part of clusters have been estimated with FRM from observations of additional radio galaxies behind these clusters (Govoni et al. 2006; Guidetti et al. 2008; Bonafede et al. 2010). To accurately constrain the magnetic fields in clusters, knowledge of the three dimensional distribution of the magnetic fields is required. This will be especially true when the Extended Very Large Array (EVLA) becomes operational, as it will be able to obtain FRM over large areas of galaxy clusters. It is also suggested that the evolution and distribution of magnetic fields in clusters may be important to the cluster formation because they play a crucial role in processes such as heat transport, which consequently affect the applicability of clusters as sensitive probes for cosmological parameters (Voit 2005). In addition, the distribution of magnetic fields can potentially serve as a tracer of the merger history of a cluster.

Magnetic field evolution is complicated and difficult to study analytically in highly non-linear systems, such as galaxy clusters, and therefore cosmological MHD simulations are used to study the properties of magnetic fields in the ICM. Although the existence of cluster-wide magnetic fields is clear, their origin is still poorly understood. Consequently, initial magnetic fields are usually added to the simulations by hand. Simulations have been performed with initial magnetic fields either from some random or uniform fields at high redshifts (Dolag et al. 2002; Dubois & Teyssier 2008; Dubois et al. 2009) or from the outflows of normal galaxies (Donnert et al. 2009). These simulations found that fields can be further

amplified by cluster mergers (Roettiger et al. 1999) and turbulence. Though it is not clear whether the initial conditions of their simulations are correct, their findings roughly match results from observations. This suggests that cosmological MHD simulations are a good way to study cluster magnetic fields. On the other hand, very small seed fields from some first principle mechanism, like Biermann battery effect have also been studied (Kulsrud et al. 1997; Xu 2009). It has been suggested that very weak seed fields can be amplified by dynamo processes in clusters (Ryu et al. 2008), though current simulations have not been able to model such processes self-consistently. In addition, the exact mechanism for dynamo is still being debated (e.g. Bernet et al. 2008).

Observationally, large scale radio jets and lobes from AGNs serve as one very intriguing source of cluster magnetic fields, because they could carry large amounts of magnetic energy and flux (Burbidge 1959; Kronberg et al. 2001; Croston et al. 2005; McNamara & Nulsen 2007). The magnetization of the ICM and the wider inter-galactic medium (IGM) by AGNs has been suggested on the energetic grounds (Colgate & Li 2000; Furlanetto & Loeb 2001; Kronberg et al. 2001), without details of the exact physical processes of how magnetic fields might be transported and amplified. Recently, using self-consistent cosmological MHD simulations, Xu et al. (2009) showed that magnetic fields from an AGN injected in a local region can be sufficient to magnetize the whole cluster to the micro Gauss level through the action of cluster mergers and the ICM turbulence. This result, which is consistent with semi-analytic models of the evolution of magnetic fields and turbulence (Subramanian et al. 2006), shows that the small-scale turbulent dynamo (Boldyrev & Cattaneo 2004; Brandenburg & Subramanian 2005) may operate in the ICM.

In this paper, we investigate the influence of injection energy and redshift on the evolution of cluster magnetic fields and their properties at the present epoch. In a following paper, we will study the magnetic field evolution of galaxy clusters with different masses and at different dynamical stages. Here, we present the properties of magnetic fields in the ICM and the distribution of synthetic Faraday rotation measurement. We also discuss the importance of high numerical spatial resolution in a large volume to follow the magnetic fields correctly in cluster formation simulations. The setup of our simulations is described in Section 2 and results are presented in Section 3. Our results are summarized in Section 4.

2. Basic Model and Simulations

Cosmological MHD simulations were performed using the newly developed ENZO+MHD code Collins et al. (2010), which is an Eulerian cosmological MHD code with adaptive mesh refinement (AMR). The initial conditions of our simulations are generated from an

Eisenstein & Hu (1999) power spectrum. The simulations use a Λ CDM model with parameters $h = 0.73$, $\Omega_m = 0.27$, $\Omega_b = 0.044$, $\Omega_\Lambda = 0.73$, and $\sigma_8 = 0.77$. These parameters are different from those used in previous simulations (Xu et al. 2009) and are close to the values from the recent WMAP observations (Spergel et al. 2007). The most important difference between simulations presented here and the previous one is the baryon to dark matter ratio, which is 14.76% (compared to 8.20% in Xu et al. (2009)). It is encouraging that the evolution of the magnetic field in this work is similar to the evolution found in Xu et al. (2009), given the differences in cluster properties and Ω_b . The simulation volume is 351 Mpc on a side, and it uses a 128^3 root grid and 2 level nested static grids in the Lagrangian region where the cluster forms. This gives an effective root grid resolution of 512^3 cells (~ 0.69 Mpc) and dark matter particles of mass resolution of $1.07 \times 10^{10} M_\odot$. As the simulation proceeds, 8 levels of refinement are allowed beyond the root grid, for a maximum spatial resolution of 11.2 kpc.

The energy of an AGN is initially injected into the ICM in the form of magnetic fields (see description in Xu et al. (2008)) over the most massive halo locally. Part of the magnetic energy, however, is quickly converted to other energies (kinetic motion and thermal energy) during the formation of radio jets and lobes in the ICM (Li et al. 2006; Xu et al. 2008). Because it is currently not possible to resolve both the galaxy cluster and the AGN environment simultaneously, we have adopted an approach that mimics the possible magnetic energy injection by an AGN (Li et al. 2006). The size of the injection region and the associated field strength are not realistic when compared to the real AGN jets, but on global scales ($>$ tens of kpc), the previous studies by Nakamura et al. (2006) and Xu et al. (2008) showed that this approach can reproduce the observed X-ray bubbles and shock fronts (e.g. McNamara et al. 2005; Nulsen et al. 2005).

The simulations were evolved from redshift $z = 30$ to $z = 0$ without radiative cooling, star formation, or feedback (so-called adiabatic). In this study, we “turn on” the AGN with magnetic fields at different redshifts of $z = 3$, $z = 2$, $z = 1$ and $z = 0.5$, centered at the most massive halo in the proto-cluster at the injection time. We have two sets of simulations. First, we have six simulations of the AGN activated at $z=3$ with different magnetic energies. The reason why our study concentrates on $z=3$ is that the comoving quasar number density peaks at $z \sim 2.5$ (e.g. Fan et al. 2001). We label simulations of this set as runs A to F, from the most to the least injected energy. The second set of simulations inject magnetic energy similar to run C, but with the injection redshift varied. Simulations with injection at $z=2$, $z=1$, $z=0.5$ are labeled as z2, z1 and z05. All the parameters of the injection model (Li et al. 2006) except the strength of the magnetic fields are kept the same for all the simulations. The magnetic energy is injected inside 40 kpc (proper not comoving) and the injection lasts for 36.7 Myr. The properties of the halo at the AGN injection and the initial and final

magnetic energies are summarized in Table 1.

AMR is applied only in a region of $(50 \text{ Mpc})^3$ where the galaxy cluster forms. During the course of cluster formation, before the magnetic fields are injected, the refinement is controlled by baryon and dark matter overdensity, which is similar to other cluster formation simulations (e.g. Motl et al. 2004; Nagai et al. 2007). After the magnetic field injection, in addition to refinement by overdensity, all the regions where the magnetic field strength is higher than $5 \times 10^{-8} \text{ G}$ are refined to the highest level. Using this refinement method, the volume that is refined to the highest level contains more than 99% of the total magnetic energy (Xu 2009). For run A, the simulation is equivalent to $\sim 600^3$ uniform grid ($\sim 600^3$ zones at the highest level) MHD runs in the cluster region with full cosmology. For cases with lower injected magnetic energy, the highly refined region will be smaller (e.g. the volume with the highest refinement of run F is about half of that of run A). The data analysis in this paper is performed using yt¹ for Enzo (Turk 2008).

3. Results

3.1. Formation History of the Galaxy Cluster

Before we discuss the properties of magnetic fields in the ICM, we present the history of the galaxy cluster formation by hierarchical mergers. The merger history determines the properties of the ICM dynamics and, in turn, the evolution of magnetic fields. In Fig. 1, we show the projected gas density at different redshifts corresponding to different stages of cluster formation for run A. The halos with AGNs injected at different redshifts are indicated by an arrow. The arrow in the $z=3$ panel applies to runs A to F, while the arrows in the $z=2$, 1, 0.5 panels apply to runs z2, z1, z05, respectively. As we will show later, the magnetic field injection does not change the halo merger properties, so we can use the same projection to indicate the AGN host halo for all simulations. Each figure is a projection of baryon density along the y direction in a box of $(16 \text{ Mpc})^3$ comoving centered at the center of the simulation domain.

Fig. 2 plot the evolution of mass and averaged kinetic energy density inside the virial radius (r_{200}) of the cluster. This shows the mass growth of the cluster and the kinetic energy available to amplify the magnetic fields. When we compute the kinetic energy, we subtract the averaged velocity of the whole cluster (the bulk motion of the cluster that cannot be used to amplify the magnetic fields).

¹<http://yt.enzotools.org>

Galaxy clusters are formed by hierarchical mergers as described by Motl et al. (2004). During the period we studied from $z=3$ to $z=0$, there are two different stages. From $z=3$ to $z=1$, the cluster is still small and increases in mass and size rapidly by frequent mergers with halos of similar sizes. From $z=3$ to 1, the mass of the cluster increases from 1.5×10^{13} to $5 \times 10^{14} M_{\odot}$. Since the mass from major mergers is added to the cluster slowly (over a few 100 Myrs), the virial mass inceases quite smoothly. Due to frequent mergers, the cluster is active and the kinetic energy density is relatively high. The peaks of the evolution of kinetic energy density show the impact of major mergers. By $z=1$, the major part of cluster has been formed. Mergers have become rare and the merging halos are relatively small compared to the central cluster, producing smaller disturbance on the ICM. Thus the mass grows at a much slower rate (a factor of 2.5 for the remaining 7 Gyr) and the cluster becomes relaxed, with a lower kinetic energy density that decreases gradually to only about one quarter its value before $z=1$. The cluster has a final virial mass of $1.25 \times 10^{15} M_{\odot}$ with a virial radius of 2.16 Mpc.

To show the influence of the magnetic fields on the cluster formation, Fig. 3 plots the projected gas density at redshift $z=0$ for runs A, C, F, z2, z1, z05, in smaller projection boxes of $(8 \text{ Mpc})^3$, while Fig. 4 shows radial profiles of their baryon density and temperature. Though the injected magnetic fields and the final field distributions are quite different for various simulations, the gas density and temperature distributions are just moderately affected, mostly in the cluster central region.. The gas density increases and the temperature decreases with both injection energy and injection time, but only at most 10%. The magnetic energy in the clusters is much smaller than the kinetic and thermal energy (see Xu et al. (2009) and Fig. 11 in Sec. 3.2.3) throughout most of the cluster. So they are dynamically unimportant during the cluster formation. The impact of magnetic fields is more visible in the inner 400 kpc but these don't change the properties of the cluster as a whole significantly.

3.2. Magnetic Field Distribution and Magnetic Energy Evolution

3.2.1. Magnetic Field Spatial Evolution

To illustrate the spatial evolution of the magnetic fields, we present the projections of magnetic energy density ($B^2/8\pi$) at different redshifts in Fig. 5 for cases with AGN “turned on” at $z=3$ and in Fig. 6 for all other cases. We set the center of the view at the cluster center at the observed time, since the magnetic fields move with the cluster as shown in Fig. 1. With the strong local injections, the magnetic fields first expand by their own pressure to form bubbles. The mergers and random motions of the ICM then destroy the bubbles

and spread the magnetic fields away from the vicinity of the injection locations to the whole cluster. These processes were described in Xu et al. (2009).

For cases with an AGN injected at $z=3$, the magnetic fields basically evolve in a similar way and are all distributed throughout a large volume of the cluster at low redshifts. The magnetic fields are spread throughout the cluster very quickly before $z=0.5$ when the cluster is more active. The strength of the initial magnetic fields determines the early expansion of the fields, thus the final field distribution. Magnetic fields in run A, with the strongest injected fields, expand the fastest at early times and are distributed in the largest volume at any stage during the cluster formation. After $z = 0.5$, the magnetic field distribution in the ICM shows signs of saturation. Note that the cluster is continuously growing in mass and undergoing minor mergers (albeit slowly). Here we regard that magnetic fields have reached a "saturated" state when they have stopped growing (or have very slow growth) both in their total energy (see Fig. 7 in the next subsection) and spatial distribution. The detailed physical processes of saturation, however, deserve a more careful evaluation, which will be presented in a future publication. Though expanding with different rates at early time, magnetic field distributions of runs B, C, and D are quite similar at $z=0$. It seems that they are all saturated at $z=0$, and this saturation level is determined more by the ICM properties than the initial magnetic field strength. For runs E and F, the magnetized regions are significantly smaller than the stronger injection energy cases, and the strength of projected magnetic fields is weaker. Their magnetic fields have more difficulty expanding in the ICM at the early time due to their weak initial magnetic pressure. This leads to a much smaller cross section for the mergers, and consequently less chance of being brought to the other parts of the cluster and to be amplified. They continue to expand to a much larger volume from $z=0.5$ to $z=0$, and don't clearly show indication of being saturated.

For AGN injected at $z=2$, which injects magnetic fields about 1 Gyr later, the magnetic fields are also spread throughout the whole cluster. Though the initial magnetic fields are injected at a different places, and with larger energy, the field distribution at $z=0$ is very similar to runs C and E. For the run with injection at $z=1$, magnetic fields still spread out of the cluster center, but are distributed in a much smaller area. This is because the injected magnetic fields miss the most active period of the cluster mergers. For run z05, though the magnetic bubbles are still destroyed, the magnetic fields are confined in the central region of the cluster. The cluster at $z=0.5$ is already quite large, so it is difficult for the merging halos to bring the magnetic fields far away from the center. For the case when the AGN injection is much later at $z=0.05$ (Xu et al. 2008), the magnetic fields could survive in a bubble morphology, which resembles observations of X-ray cavities in clusters.

3.2.2. Magnetic Energy Evolution

Since we have only one source of magnetic fields in each simulation, it is straight forward to track the history of magnetic energy amplification in the cluster. The evolution of the total magnetic energy of all the simulations is shown in Fig. 7.

The magnetic energy generally decreases rapidly initially for a few hundred million years because of the rapid expansion of the magnetic structure. For AGN injected before the main mergers (runs A-F, z2 and z1), the magnetic energy gradually increases due to the combined effects of major mergers and the ICM turbulence until saturation occurs or the simulation ends.

At $z = 0$, the total magnetic energy is $(14, 9.6, 6.5, 7.3, 5.1, 2.9) \times 10^{60}$ ergs, for runs A-F with a gain of about 10, 15, 40, 150, 400, and 900 times, respectively. It is interesting that the magnetic energy of run F, which has an injected energy of just 3×10^{57} ergs, or one-thousandth of the magnetic energy injected in run A, is one quarter the energy of run A at the final stage. So a small amount of magnetic fields from AGNs can still be amplified to magnetize the whole cluster to the observed level, provided that the ICM turbulence is strong.

For the later injection cases, the situations can be quite different. For z05, the magnetic energy never increases, and drops to 7×10^{57} ergs at $z=0$. As shown in the magnetic field distribution, since the magnetic fields are put into the system too late, there is not enough time, or enough mergers, to distribute the magnetic fields to large volumes. For the other two runs, z2 and z1, the magnetic fields still have enough time to expand and get amplified in the ICM turbulence. Their magnetic energy increases in a very similar way to cases of the injections at $z=3$. Run z1 has a final magnetic energy of 10^{60} ergs, and the magnetic energy evolution of z2 is almost identical to the run C after 3 Gyr, and seems saturated.

3.2.3. Radial Profiles of Magnetic Fields

In Fig. 8, we present the spherically averaged radial profiles of RMS magnetic field strength at low redshifts of runs A to F. By $z=1$, the strong initial magnetic field of run A allow it to reach the μG level, and fill the virial radius of the cluster. By $z=0.5$, all runs A-F have field strengths of $> 1\mu\text{G}$ at the cluster center. By $z=0$, only the run with the weakest initial field strength, run F, has not filled the virial radius.

From $z=1$ to $z=0$, the magnetic field gradually saturates with the ICM motions from the center of the cluster to the virial radius. Magnetic field strength in the cluster center is

maintained at the micro Gauss level, while at larger radii, the field strength is continues to be amplified. There is a clear trend that the slope of the radial profile decreases with time. In run A, the magnetic field strength at the virial radius remains at a relatively constant value of $0.2\text{--}0.5\ \mu\text{G}$ from $z=0.5$ to $z=0$. The magnetic field strength in the other cases continues to be amplified at the virial radius in this reshift interval, and their field strength profiles in these runs approach the distribution in run A. The run with the weakest injected magnetic field strength, run F, has its field amplified fastest, and over the widest range of radii. It seems that the profiles of magnetic fields are decided by the ICM motions, rather than the initial magnetic field strength, provided there is enough time for the magnetic field to be mixed throughout the cluster and amplified by the turbulence.

Fig. 9 shows the radial profiles of magnetic field strength at $z=0$ for simulations with magnetic field injected after $z=3$. The magnetic fields of z2 are also higher than $1\ \mu\text{G}$ and have almost the same profile as run C, except in the central 100 kpc. For run z1, the magnetic field strength is well distributed through most of the cluster and gets amplified, while the final field strength is at the micro Gauss level, and spread out to more than 1.5 Mpc away from the center. But since there is less time for the field to be amplified in the outer part of the cluster, the radial profile is steeper. The magnetic fields of z05 is much weaker and locally distributed. It shows that the magnetic field injected this late are not likely to be an important sources of cluster magnetic fields.

At $z = 0$, the magnetic field strengths in all cases injected before $z=1$ are at the micro Gauss level at the cluster center, and extend to large radii. Magnetic field strength profiles in these cases tend to a power law, with best fit slope of -0.6 between $r = 0.2$ to $2\ \text{Mpc}$. This is flatter than magnetic profiles seen in some other simulations (Dolag et al. 2002; Donnert et al. 2009). One possible reason for the flatter radial profiles in our simulations is that we maintain a high resolution in regions with lower density but significant magnetic field strength. We have also performed a simulations with a less aggressive set of refinement criteria, the usual refinement criteria of gas and dark matter overdensity. This causes lower resolution in the outer regions, where the density is low but the magnetic field is significant. We see a faster drop in magnetic field strength with lower resolutions at large radius (details will be discussed in Sec. 3.5). The difference in profiles could also be caused by the different initial magnetic fields used in our simulations (vs uniform initial fields, for example). For instance, the gas collapse plays a less important role in the magnetic field amplifications in our simulations, since there is no magnetic field initially in the collapsing gas.

3.2.4. Magnetic Field Volume Distribution

In Fig. 10, we plot the volume histograms of magnetic field strength of the central 1 Mpc sphere to demonstrate the spatial distribution of the magnetic fields. Magnetic fields are mixed with the ICM plasma very well for all cases with injections before $z=2$. More than 90% of the ICM volume is populated with magnetic fields $\geq 0.1 \mu\text{G}$. The peak of magnetic field strength distribution increases with stronger or earlier magnetic field injections. On the other hand, magnetic fields of run z05 are very weak and fill less than 10% of the volume.

Figure 11 illustrates the volume histograms of the plasma β ($=nk_B T / \frac{B^2}{8\pi}$) at $z=0$ for the same volume. The thermal energy is always much larger than the magnetic energy. The peak of the β distribution is at ~ 500 for run A. The fact that $\beta \gg 1$ for these runs indicates that in most of the region, magnetic fields are dynamically unimportant and follow the gas passively.

To show the correlation between the gas density and the strength of magnetic fields, we plot in Fig. 12 the two-dimensional distribution of the magnetic field strength vs. the gas density at $z=0$ for runs A, C, F, z2, z1, and z05. There is no obvious correlation between the field strength and the gas density. The distribution is similar for the first five cases. Most of the magnetic field strength is between 0.1 to a few micro Gauss, and are mixed with plasmas with a wide range of densities. This is because the magnetic fields are originally injected in a small volume and are randomly spread through the gas and amplified by the ICM turbulence. So the field strength does not scale as $\rho^{2/3}$, as in it would if the magnetic field was initially distributed in a large volume and mostly amplified by collapse. This property may be used to distinguish different magnetic field origins. The magnetic field strength in z05 is very weak and mostly confined to the high density cluster core region.

3.3. Energy Power Spectrum and Small Scale Dynamo with MHD Turbulence

The top panel of Fig. 13 plots the power spectra of kinetic and magnetic energy density of a box of 512^3 ($\sim (5.5 \text{ Mpc})^3$ comoving) enclosing the cluster for run A at different redshifts. The kinetic power spectra grow rapidly from $z=2$ to $z=1$ during the active merger period of the cluster formation, then remain relatively constant level for the rest of the simulation. The kinetic power spectra show a smooth power law similar to a Kolmogorov-like spectrum for incompressible turbulence in the range $k \sim 0.01\text{-}0.1 \text{ kpc}^{-1}$. They are similar to the spectra obtained from pure hydrodynamic simulations (Vazza et al. 2009). The spectrum steepens gradually for $k > 0.1$ on small scales due to several effects: the damping of kinetic energy by the shocks (Stone et al. 1998); the back reaction of magnetic fields, especially at low

redshifts when the magnetic energy density is close to the kinetic energy density at those scales; and numerical diffusion. The magnetic energy power spectra at large scales follow the $k^{3/2}$ Kazantsev law. At early times, when the magnetic energy density is much smaller than the kinetic energy density at all scales, the magnetic energy grows exponentially in all scales. The power laws of both the kinetic and magnetic energy, and the exponential growth of magnetic energy clearly show that the small scale dynamo is operating in the ICM (see Brandenburg & Subramanian 2005). The characteristic timescale for magnetic energy growth is the eddy turnover time at the dissipation scale (at $k \sim 0.1$ to 0.2 kpc^{-1} in this simulation), which is $\sim 1 \text{ Gyr}$ from $z=2$ to $z=1$, and increases gradually to 3 Gyr at $z=0$. With the rapid growth from $z=2$ to $z=0.5$, the magnetic energy density reaches equipartition with the kinetic energy density at small scales. Then, the operation of small scale dynamo goes into the second stage. During this stage, the magnetic energy grows linearly with a rate proportional to the turbulence energy cascade rate (Schekochihin & Cowley 2007) and the peak of magnetic energy moves to larger scales (Cho & Vishniac 2000). The characteristic timescale is again the eddy turnover time at the dissipation scale, which is $\sim 2 \text{ Gyr}$ at $z=0.5$ and is longer than 3 Gyr at $z=0$. The longer eddy turnover time is due to the relaxation of the cluster. The linear growth of magnetic energy happens between $z=0.37$ and $z=0.16$ at a rate of $\sim 1.5 \times 10^{60} \text{ ergs/Gyr}$. After that, the magnetic energy stops growing and even decreases slowly. We consider the magnetic fields saturated at this time, even though the magnetic and kinetic energy have not reached equipartition globally. Here, the saturation of magnetic fields happens when the operation of small scale dynamo is in the linear growth stage and the relaxation of the cluster makes this linear growth of magnetic energy very slow with the long eddy turnover time.

The magnetic power spectra of six runs of the same volume at $z=0$ are plotted in the bottom panel of Fig. 13. We don't show the kinetic power spectra since they are all almost the same as that of run A. However, the magnetic power spectra for different runs are at quite different levels. All the magnetic energy density power spectra show a power law $k^{3/2}$ over a small range, except for run z05, so the magnetic fields are indeed amplified by the small scale dynamo process in all these runs. Magnetic fields in simulations with weaker initial magnetic fields or later injection need more time to spread throughout the cluster, and occupy relatively smaller volumes, especially for runs F and z1. The evolution of magnetic energy shows that the magnetic fields of runs C and z2 are also in the second stage of small scale dynamo with the linear growth. The magnetic energy density of these runs saturates at a subequipartition level with respect to the kinetic energy density for $k > 0.3 \text{ kpc}^{-1}$, which is likely because their magnetic fields fill smaller volumes of the cluster. The magnetic energy of run F and z1 continues to exponentially grow for $z < 0.5$ with a lower rate due to the longer eddy turnover time and does not clearly show whether or not the increase becomes

linear at $z \sim 0$. For run z05, there are not enough big mergers to spread the fields to large enough volume to catch the turbulence motions. Even though there has been 6 Gyr since the AGN input, its power spectrum shows no sign of the operation of the small scale dynamo.

Even though we have solved the ideal MHD equations in our simulations, there is numerical diffusion that has allowed the turbulence to damp and the magnetic fields to diffuse in the ICM. The rate of diffusion is determined by the numerical Reynolds number and magnetic Reynolds number. We estimated that these numbers in our simulations are on the order of a few hundred. The real ICM could have Reynolds number is on the order of 100 or may be bigger (up to ~ 1000) if magnetic fields are present (Sunyaev et al. 2003), which is close to our simulations. But its magnetic Reynolds number is not well determined, especially in a magnetized turbulent medium. The small scale dynamo theory and simulations (Haugen et al. 2004) have shown that the dynamo will operate under our simulation conditions. Most of the previous research of the small scale dynamo is in incompressible turbulence limit. For the ICM, the compression by shocks generated by mergers are very frequent and important, and they could modify the turbulence properties. This in turn could affect the operation of the small scale dynamo. Further study on the small scale dynamo in compressible turbulence is needed.

3.4. Faraday Rotation Measurement

Another important observational description of magnetic fields in the ICM is the FRM. The RM maps are used not only to determine the strength of magnetic fields but also the turbulent structure of them (Enßlin & Vogt 2006). For a distant polarized source, the FRM, which is defined as ratio of change of polarization angle to wavelength squared, in unit of rad m^{-2} , is (Kronberg et al. 2008):

$$RM(z_s) = \frac{\delta\chi}{\lambda^2} = 8.1 \times 10^5 \int_0^{z_s} \frac{n_e(z)B_{||}(z)}{(1+z)^2} \frac{dl}{dz} dz, \quad (1)$$

where n_e is free electron number density in cm^{-3} , $B_{||}$ is the line of sight component of magnetic fields in Gauss, and dl/dz is the comoving path increment per unit redshift in parsec. We compute the synthetic FRM maps by integrating 8 Mpc along each axis. The RM maps observed from different directions are quite similar, so we only show the results along the y axis here. Fig. 14 shows the spatial distribution of FRM at $z = 0$ for six cases. The RM maps of runs with different initial field strengths or of different injection times have similar features but are different in details. Interestingly, the FRM map shows not only the small scale variations reminiscent of the ICM MHD turbulence, but also show long, narrow filaments, which may be relics of recent mergers. There are some high $|RM|$ regions at the

outer part of the cluster, which are consistent with the $> 100 \text{ rad m}^{-2}$ RM observed far from the cluster center in Abell 2255 (Govoni et al. 2006) and Coma cluster (Bonafede et al. 2010). For run z05, the FRM not only covers the smallest area, but has much less small-scale structure, which is because the magnetic fields has had little amplification on small scales.

In Fig. 15, we present the circularly averaged radial profiles of the absolute value of RM ($|RM|$), which is $\frac{1}{2\pi} \int_0^{2\pi} |RM| d\Phi$, where Φ is the azimuth angle, and the radial profiles of the standard deviations of RM, which is $(\frac{1}{2\pi} \int_0^{2\pi} (RM - \overline{RM})^2 d\Phi)^{1/2}$, where $\overline{RM} = \frac{1}{2\pi} \int_0^{2\pi} RM d\Phi$. All the $|RM|$ profiles are self-similar except for z05. The $|RM|$ of run A are as high as 1000 rad m^{-2} at the center, then drop gradually with increasing radius to a few rad m^{-2} at 2 Mpc. The central $|RM|$ of runs F and z1 are just above 300 rad m^{-2} . The RM values are sensitive to the initial magnetic fields. With much weaker fields, the $|RM|$ of z05 are very small and only present in the core region. The RM vary quickly on small scales, so their standard deviations are large.

We also show the histograms of RM and the cumulative histograms of $|RM|$ inside a circle of 500 kpc in Fig 16. For the cases with magnetic fields injected at $z=3$, significant RM covers a large portion of the area. Only $\sim 10\%$ of the area is covered with RM close to zero for run A, and just above 20% for run F. The positive and negative RM are roughly symmetric. In run A, the average and standard deviation of RM of this area are -4.09 rad m^{-2} and $307.75 \text{ rad m}^{-2}$, respectively. There is a significant fraction of the area covered with $|RM|$ larger than 500 rad m^{-2} .

The general features of RM distributions of our simulations are consistent with the observations of galaxy clusters (e.g. Kim et al. 1991; Eilek & Owen 2002). But since present observations can only measure FRM on small areas in a cluster, due to the limited number of the observed radio sources behind or embedded in a cluster, it is too early to make a detailed comparison between the distributions of RM in our simulations and observations. We expect the comparison will be available soon, when many more radio sources will be observed by EVLA.

3.5. Importance of Simulation Resolutions on Magnetic Field Evolution

We find that the additional refinement criterion of magnetic field strength is very important in following the magnetic fields correctly in our simulations. With only refinement by the baryon and dark matter overdensity, the spatial resolution in the outer part of the cluster drops quickly with increasing radius. This leads to numerical reconnection in low resolution regions, which will destroy magnetic fields. We reran run A without the magnetic

field refinement to test the importance of resolution. Results are given in Fig. 17 and 18.

Without high resolution in a large volume, the simulation cannot resolve the turbulent motions, and in turn, cannot capture the small-scale dynamo effect. In addition, the magnetic fields suffer much larger numerical dissipation with the lower resolutions. The magnetic energy in the low resolution run keeps decreasing after injection until the end of simulation. The few small increases in magnetic energy that do occur correspond to major mergers. During the early stage, the magnetic energy drops much faster in the lower resolution run, because most of the magnetic fields numerically reconnect in low resolution regions. The amplification of the magnetic field fails, most likely because the small scale turbulent motions needed by the dynamo process are not captured by this simulation in a large enough volume. When the simulations end at $z = 0$, there are 5000 times more magnetic energy in the case with magnetic refinement.

Though the magnetic energy evolution is very different for different refinement criteria, the cluster still forms in a similar way. At $z = 0$, the radial profiles of the baryon density and temperature are almost the same. For density, there is only small difference out to 400 kpc due to the decrease of resolutions in the no magnetic refinement run. The temperature profiles are different between 200 and 600 kpc, which may be related to the differences caused by resolving the merger shocks with different resolutions. But the magnetic field strength profiles are totally different for these two simulations. Even in the central region with the highest resolution, the magnetic field strength of the lower resolution case is below $0.1 \mu\text{G}$, which is much weaker than that of the well refined one. Since both simulations have the same resolution in the core region, up to 50 kpc radius, the dramatic difference in the field strength shows that the magnetic fields amplified in the outer regions of the cluster and transported inwards play a large role in the magnetic field strength in the cluster core. The radial profile of the run without magnetic field refinement is also steeper than that of the magnetic refinement one.

This clearly shows that the simulation resolution is very important to the magnetic field evolution in the case when magnetic fields are initially injected in a local region. Simulations without high resolution in a large enough region will fail to capture the small-scale dynamo process, and lose most of the magnetic field. Whether different seeding processes, for example with initial magnetic fields everywhere, will have similar effect is still unclear. We are performing some simulations to address this issue.

Though the current spatial resolution of our simulations is enough to capture the operation of the small scale dynamo in the ICM, we don't know whether the simulation is converged. With current computational capability, we can't have simulations with even higher spatial resolutions in a large enough volume to test convergence. Our current results

should be taken only as the lower bound of magnetic fields in the ICM. We will study the convergence of these simulations once the computation becomes possible.

4. Summary

In this work, we have described the magnetic field evolution and properties of the ICM with simulations in which magnetic energy was injected by an AGN outburst. We are encouraged by the similarities seen in field evolution as compared to our earlier work (Xu et al. 2009), which used a completely different galaxy cluster, and magnetic energy injected at different strengths and at different times. Using magnetic fields from active galaxies and further amplifying them by the ICM motions is a robust way to populate the cluster with magnetic fields. On the other hand, since we have not verified whether the numerical convergence is reached in our simulations due to the limit of computational power, the magnetic fields obtained in this paper should be treated as the minimal possible magnetic fields in the ICM.

We have simulated the AGN injection with a wide range of magnetic energy between 10^{57} and 10^{60} ergs, which covers the typical range of energy output of radio galaxies (Kronberg et al. 2001). It is interesting that, with the huge range in injected magnetic field strength, the galaxy cluster is magnetized to a similar level, especially at the cluster central regions. The magnetic energy is amplified by more than 900 times in the case with the least initial magnetic field injection. Magnetic energy growth of some runs seems to saturate at low redshift. The saturated magnetic fields in the cluster center are at the micro Gauss level, which is consistent with observed magnetic field strengths, as measured by different observational methods. Further study is needed to understand the saturation mechanism and why the magnetic fields saturate with magnetic energy at a few percent of the kinetic energy (Xu et al. 2009; Xu 2009).

We also report simulations with magnetic fields injected at different redshifts. We find that magnetic fields injected as late as $z=1$ can still effectively magnetize the cluster, while the magnetic fields from AGNs after $z=0.5$ will not contribute substantially to the cluster wide magnetic fields. So as long as the magnetic fields are injected into the cluster before the major mergers in its formation history, the cluster will be significantly magnetized.

Since more injected magnetic energy doesn't necessarily correspond to significantly higher final magnetic energy, additional initial magnetic fields from multiple AGNs or from other sources (e.g. normal galaxies or early universe) may not necessarily change the magnetic field strength in a cluster. We have performed a simulation with two AGN injections

(each injected in different halos with magnetic energy similar to run D). Its final magnetic energy (7.62×10^{60} ergs) and the magnetic field profile are very similar to the single injection result. These results will be presented in a future publication.

The injected local magnetic fields mix with the ICM efficiently by the mergers and the turbulent ICM motions. In all cases except z05, the volume filling factors are quite high. The magnetic fields fill the central region of the cluster up to 1 Mpc. The magnetic field strength is not strongly correlated with the gas density, as the fields are distributed through a large range of gas density.

We have produced FRM maps of the whole cluster based on our simulation results. They have similar features as the observed cluster RM (e.g. Taylor & Perley 1993; Eilek & Owen 2002; Guidetti et al. 2008). More detailed comparisons need to wait for the additional observational results from the EVLA.

We thank S. Colgate and H. Aluie for discussions. This work was supported by the LDRD and IGPP programs at LANL and by DOE/Office of Fusion energy Science. Computations were performed using the institutional computing resources at LANL. ENZO_MHD is developed at the Laboratory for Computational Astrophysics, UCSD with partial support from NSF grants AST-0708960 and AST-0808184 to M.L.N.

REFERENCES

- Bernet, M. L., Miniati, F., Lilly, S. J., Kronberg, P. P., & Dessauges-Zavadsky, M. 2008, *Nature*, 454, 302
- Boldyrev, S., & Cattaneo, F. 2004, *Physical Review Letters*, 92, 144501
- Bonafede, A., Feretti, L., Murgia, M., Govoni, F., Giovannini, G., Dallacasa, D., Dolag, K., & Taylor, G. B. 2010, *A&A*, 513, A30
- Brandenburg, A., & Subramanian, K. 2005, *Phys. Rep.*, 417, 1
- Burbidge, G. R. 1959, *ApJ*, 129, 849
- Carilli, C. L., & Taylor, G. B. 2002, *ARA&A*, 40, 319
- Cho, J., & Vishniac, E. T. 2000, *ApJ*, 538, 217

- Colgate, S. A., & Li, H. 2000, in IAU Symposium, Vol. 195, Highly Energetic Physical Processes and Mechanisms for Emission from Astrophysical Plasmas, ed. P. C. H. Martens, S. Tsuruta, & M. A. Weber, 255–264
- Collins, D. C., Xu, H., Norman, M. L., Li, H., & Li, S. 2010, *ApJS*, 186, 308
- Croston, J. H., Hardcastle, M. J., Harris, D. E., Belsole, E., Birkinshaw, M., & Worrall, D. M. 2005, *ApJ*, 626, 733
- Dolag, K., Bartelmann, M., & Lesch, H. 2002, *A&A*, 387, 383
- Donnert, J., Dolag, K., Lesch, H., & Müller, E. 2009, *MNRAS*, 392, 1008
- Dubois, Y., Devriendt, J., Slyz, A., & Silk, J. 2009, *MNRAS*, 399, L49
- Dubois, Y., & Teyssier, R. 2008, *A&A*, 482, L13
- Eilek, J. A., & Owen, F. N. 2002, *ApJ*, 567, 202
- Eisenstein, D. J., & Hu, W. 1999, *ApJ*, 511, 5
- Enßlin, T. A., & Vogt, C. 2006, *A&A*, 453, 447
- Fan, X., Strauss, M. A., Schneider, D. P., Gunn, J. E., Lupton, R. H., Becker, R. H., Davis, M., Newman, J. A., Richards, G. T., White, R. L., Anderson, Jr., J. E., Annis, J., Bahcall, N. A., Brunner, R. J., Csabai, I., Hennessy, G. S., Hindsley, R. B., Fukugita, M., Kunszt, P. Z., Ivezić, Ž., Knapp, G. R., McKay, T. A., Munn, J. A., Pier, J. R., Szalay, A. S., & York, D. G. 2001, *AJ*, 121, 54
- Feretti, L. 1999, in Diffuse Thermal and Relativistic Plasma in Galaxy Clusters, ed. H. Boehringer, L. Feretti, & P. Schuecker, 3–8
- Ferrari, C., Govoni, F., Schindler, S., Bykov, A. M., & Rephaeli, Y. 2008, *Space Sci. Rev.*, 134, 93
- Furlanetto, S. R., & Loeb, A. 2001, *ApJ*, 556, 619
- Giovannini, G., Bonafede, A., Feretti, L., Govoni, F., Murgia, M., Ferrari, F., & Monti, G. 2009, *A&A*, 507, 1257
- Govoni, F., Murgia, M., Feretti, L., Giovannini, G., Dolag, K., & Taylor, G. B. 2006, *A&A*, 460, 425
- Guidetti, D., Murgia, M., Govoni, F., Parma, P., Gregorini, L., de Ruiter, H. R., Cameron, R. A., & Fanti, R. 2008, *A&A*, 483, 699

- Haugen, N. E. L., Brandenburg, A., & Dobler, W. 2004, *Phys. Rev. E*, 70, 016308
- Kim, K.-T., Kronberg, P. P., & Tribble, P. C. 1991, *ApJ*, 379, 80
- Kronberg, P. P., Bernet, M. L., Miniati, F., Lilly, S. J., Short, M. B., & Higdon, D. M. 2008, *ApJ*, 676, 70
- Kronberg, P. P., Dufton, Q. W., Li, H., & Colgate, S. A. 2001, *ApJ*, 560, 178
- Kulsrud, R. M., Cen, R., Ostriker, J. P., & Ryu, D. 1997, *ApJ*, 480, 481
- Li, H., Lapenta, G., Finn, J. M., Li, S., & Colgate, S. A. 2006, *ApJ*, 643, 92
- McNamara, B. R., & Nulsen, P. E. J. 2007, *ARA&A*, 45, 117
- McNamara, B. R., Nulsen, P. E. J., Wise, M. W., Rafferty, D. A., Carilli, C., Sarazin, C. L., & Blanton, E. L. 2005, *Nature*, 433, 45
- Motl, P. M., Burns, J. O., Loken, C., Norman, M. L., & Bryan, G. 2004, *ApJ*, 606, 635
- Nagai, D., Vikhlinin, A., & Kravtsov, A. V. 2007, *ApJ*, 655, 98
- Nakamura, M., Li, H., & Li, S. 2006, *ApJ*, 652, 1059
- Nulsen, P. E. J., McNamara, B. R., Wise, M. W., & David, L. P. 2005, *ApJ*, 628, 629
- Roettiger, K., Stone, J. M., & Burns, J. O. 1999, *ApJ*, 518, 594
- Ryu, D., Kang, H., Cho, J., & Das, S. 2008, *Science*, 320, 909
- Schekochihin, A., & Cowley, S. 2007, in *Magnetohydrodynamics - Historical Evolution and Trends*, ed. S. Molokov, R. Moreau, & H. Moffatt (Berlin: Springer) 85
- Spergel, D. N., Bean, R., Doré, O., Nolta, M. R., Bennett, C. L., Dunkley, J., Hinshaw, G., Jarosik, N., Komatsu, E., Page, L., Peiris, H. V., Verde, L., Halpern, M., Hill, R. S., Kogut, A., Limon, M., Meyer, S. S., Odegard, N., Tucker, G. S., Weiland, J. L., Wollack, E., & Wright, E. L. 2007, *ApJS*, 170, 377
- Stone, J. M., Ostriker, E. C., & Gammie, C. F. 1998, *ApJ*, 508, L99
- Subramanian, K., Shukurov, A., & Haugen, N. E. L. 2006, *MNRAS*, 366, 1437
- Sunyaev, R. A., Norman, M. L., Bryan, G. L. 2003, *Astronomy Letters*, 29, 783
- Taylor, G. B., & Perley, R. A. 1993, *ApJ*, 416, 554

- Turk, M. 2008, in Proceedings of the 7th Python in Science Conference, ed. G. Varoquaux, T. Vaught, & J. Millman, Pasadena, CA USA, 46 – 50
- Vazza, F., Brunetti, G., Kritsuk, A., Wagner, R., Gheller, C., & Norman, M. 2009, *A&A*, 504, 33
- Vogt, C., & Enßlin, T. A. 2003, *A&A*, 412, 373
- Voit, G. M. 2005, *Reviews of Modern Physics*, 77, 207
- Xu, H. 2009, PhD thesis, University of California, San Diego
- Xu, H., Li, H., Collins, D., Li, S., & Norman, M. L. 2008, *ApJ*, 681, L61
- Xu, H., Li, H., Collins, D. C., Li, S., & Norman, M. L. 2009, *ApJ*, 698, L14

Table 1: Halo Properties and Magnetic energy of simulations.

Runs	Injection z	Halo Properties				Magnetic Energy	
		$r_{200}(Mpc)$	$M_{vir}(M_{\odot})$	$M_{gas}(M_{\odot})$	$M_{DM}(M_{\odot})$	Injected (ergs)	z=0 (ergs)
A	3	0.189	1.50e13	2.14e12	1.28e13	1.94e60	1.43e61
B	3	same as above				6.17e59	9.55e60
C	3					1.85e59	6.48e60
D	3					4.98e58	7.25e60
E	3					1.27e58	5.13e60
F	3					3.20e57	2.86e60
z2	2	0.386	5.71e13	7.33e12	4.98e13	1.46e59	5.83e60
z1	1	1.11	4.89e14	6.77e13	4.21e14	1.47e59	9.47e59
z05	0.5	1.53	7.28e14	1.03e14	6.24e14	1.68e59	6.45e59

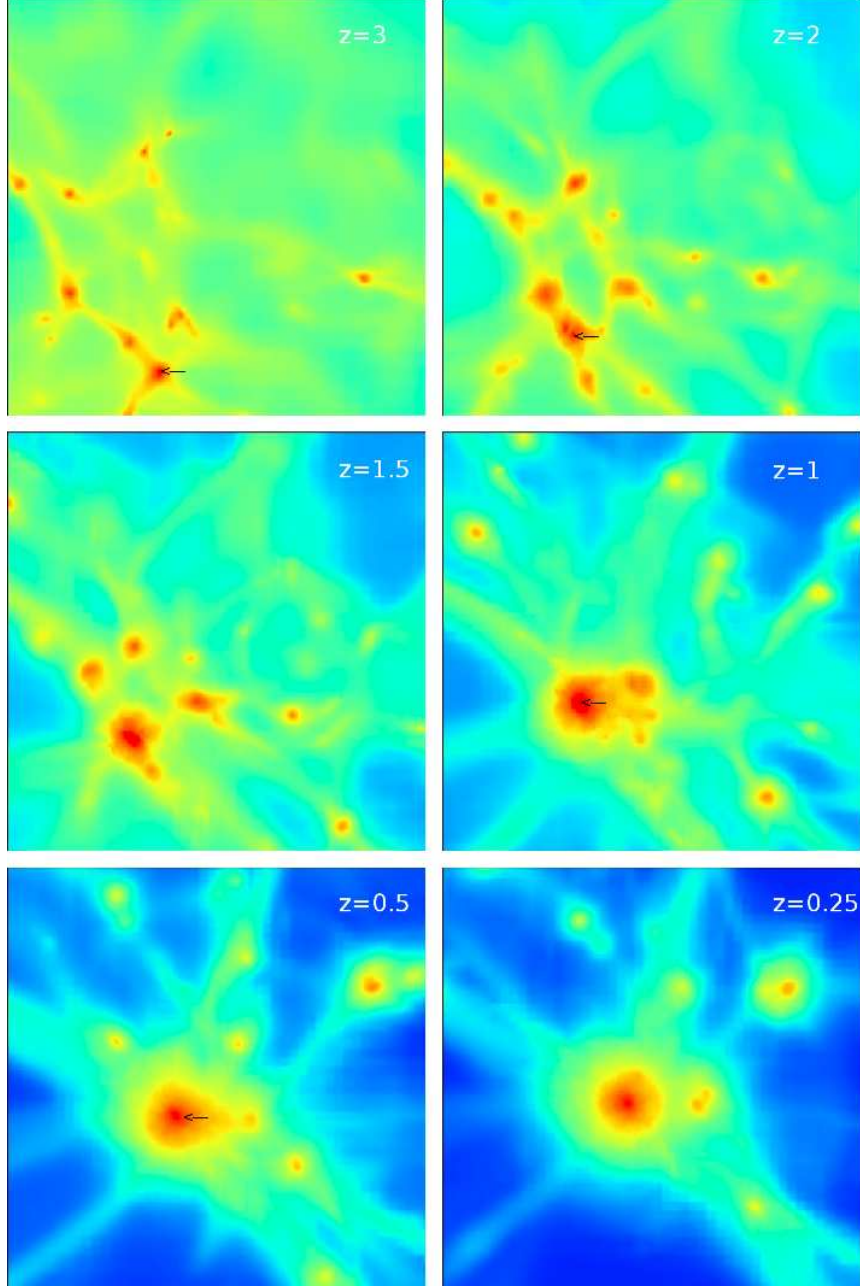


Fig. 1.— Snap shots of the projected baryon density for different epochs of the formation history of run A. Each image covers a region of 16 Mpc \times 16 Mpc (comoving) at the simulation domain center. The projected results are obtained by integrating 16 Mpc (comoving) centered at the simulation center along lines perpendicular to the observed plane. The six columns are marked with the respective redshift as $z = 3, 2, 1.5, 1, 0.5, 0.25$. The color range is from 1.0×10^{-5} to 1.0×10^{-1} g cm $^{-2}$ for the baryon density.

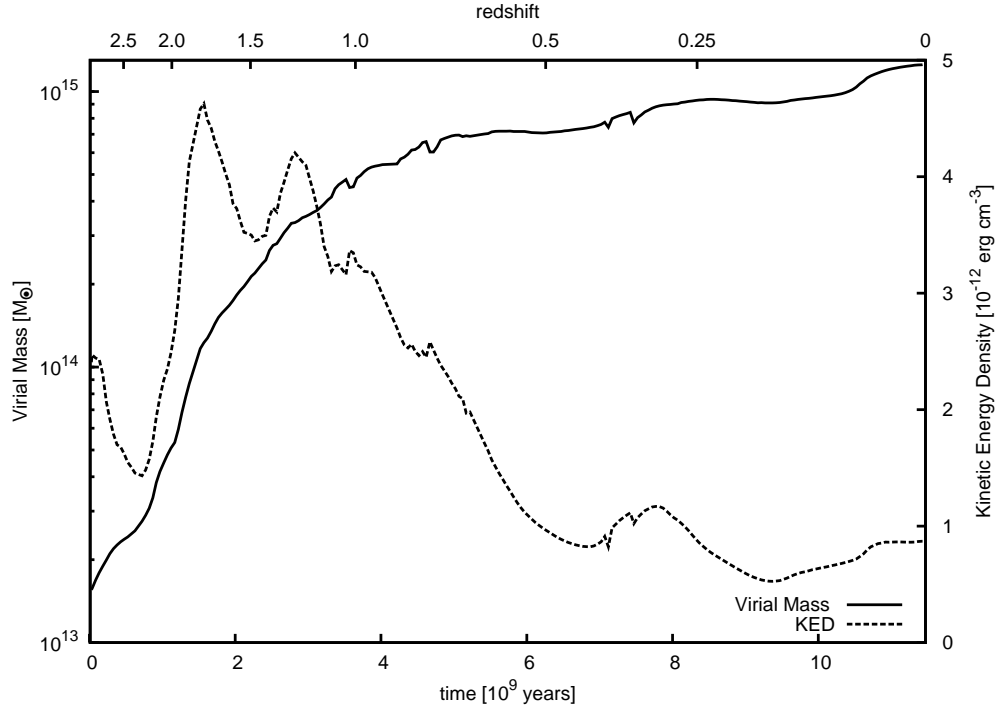


Fig. 2.— Virial mass and averaged kinetic energy density inside the virial radius as function of time of run A. The mass of the galaxy cluster increases rapidly before 5 Gyr due to many mergers, so the kinetic energy density remains high. After $z=1$, both the mass growth rate and the kinetic energy density drop because the merging halos are relatively small compared to the whole cluster.

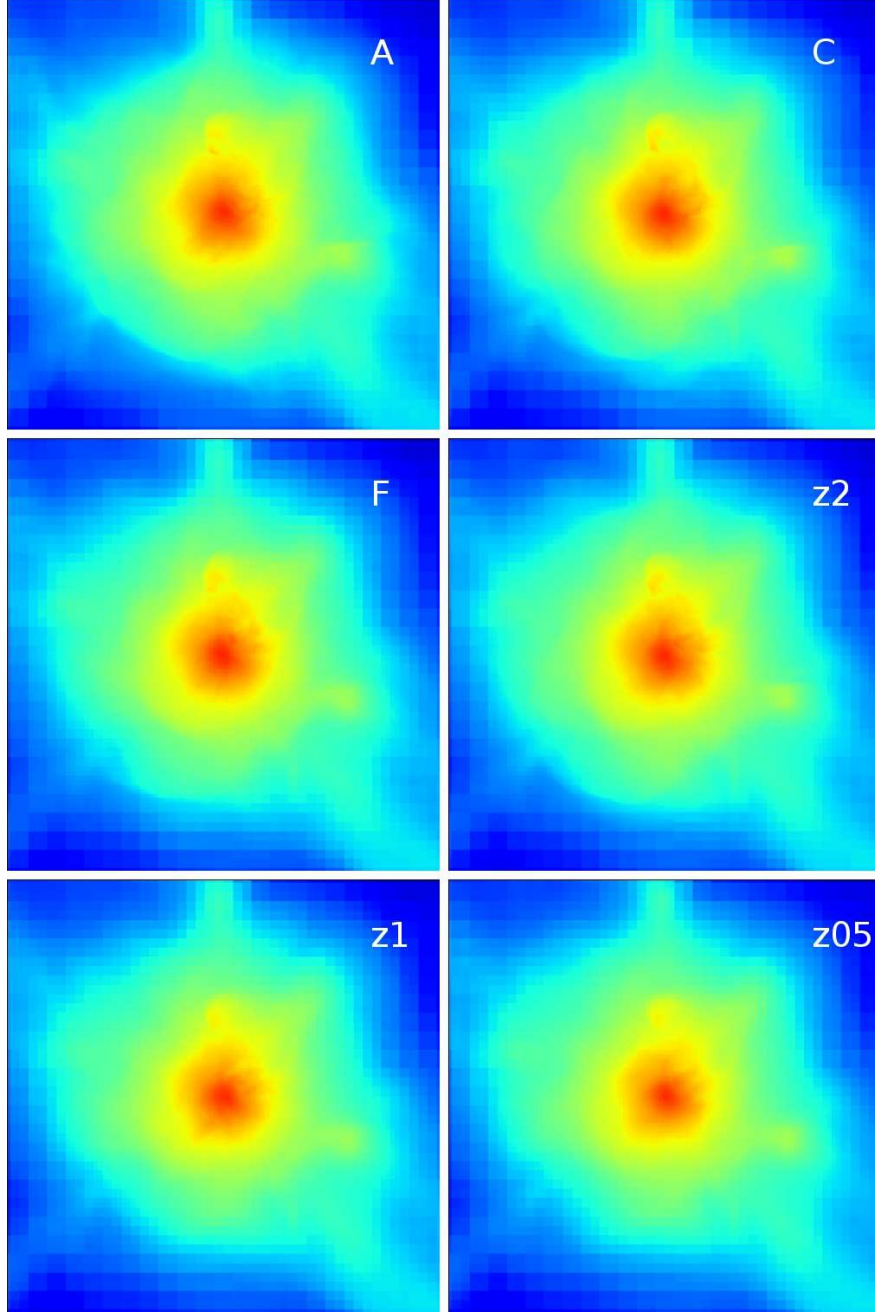


Fig. 3.— Projected baryon density for different injection levels of magnetic energy at $z = 0$. Each image covers a region of $8 \text{ Mpc} \times 8 \text{ Mpc}$. The projected results are obtained by integrating 8 Mpc centered at the simulation center along lines perpendicular to the observed plane. The panels are marked with the respective cases. The color range is from 1.0×10^{-5} (blue) to 1.0×10^{-1} (red) g cm^{-2} .

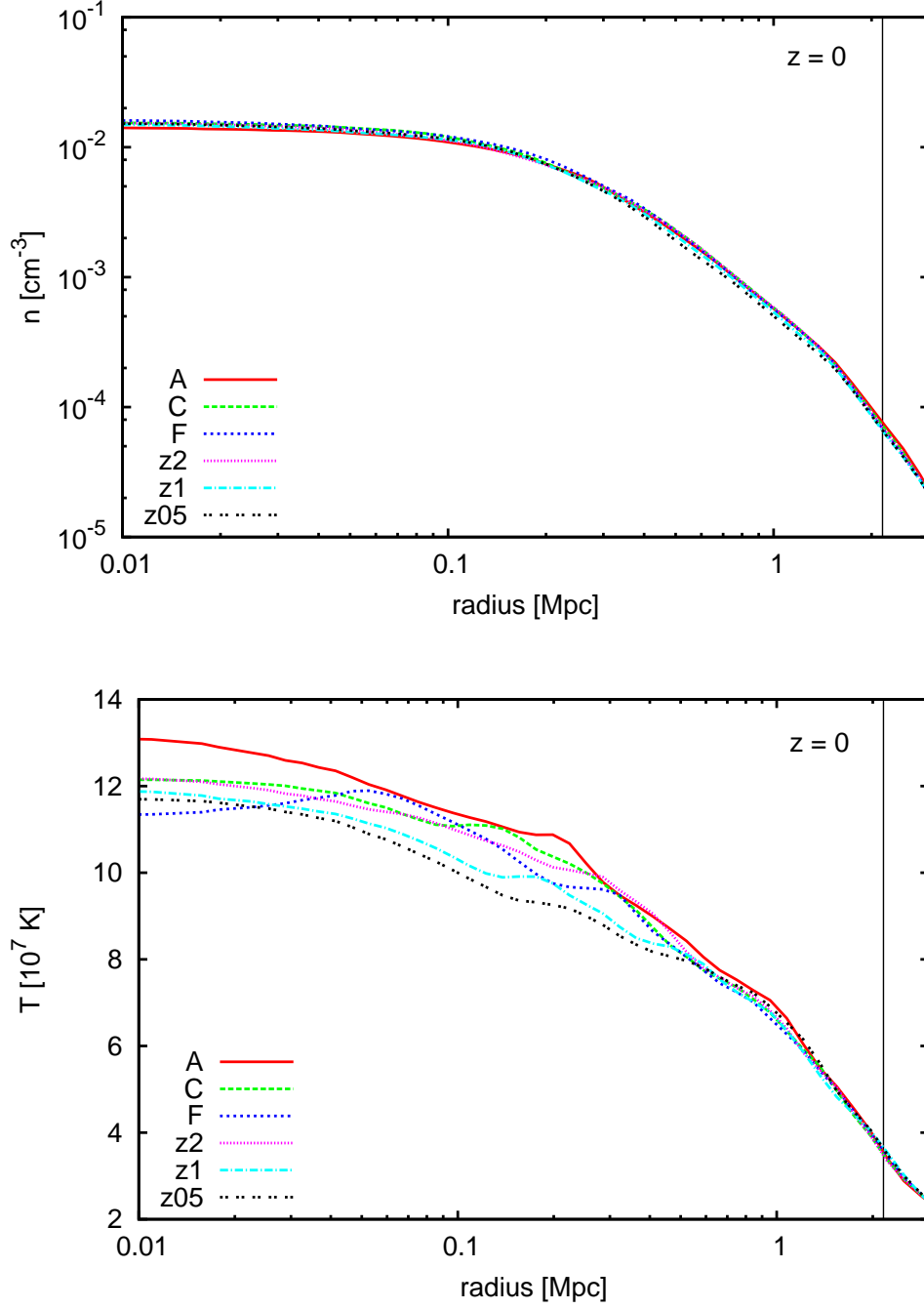


Fig. 4.— Spherically averaged radial profiles of the gas density and temperature at $z=0$. The magnetic fields have small impact on the density and temperature profiles over the cluster central region. The solid vertical line shows the virial radius.

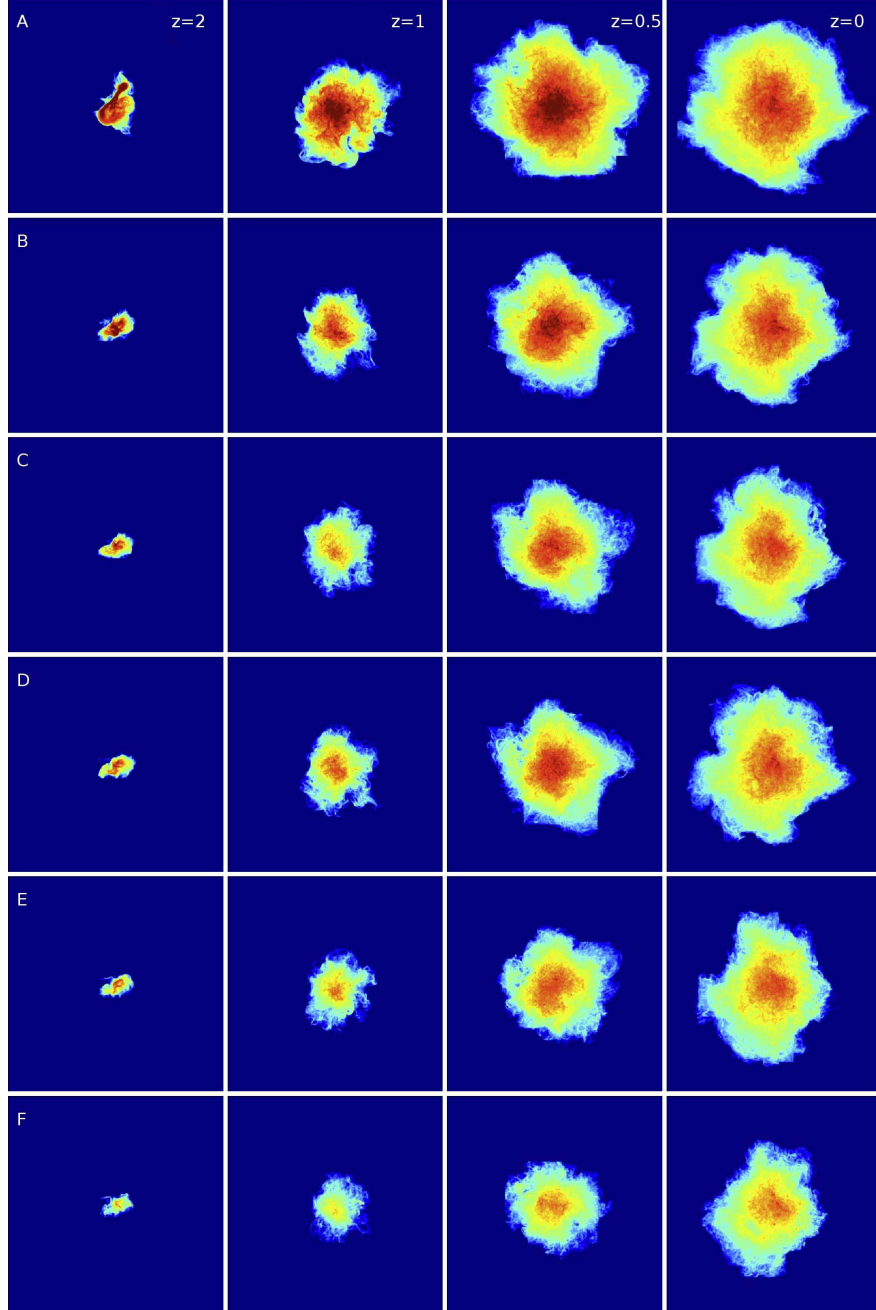


Fig. 5.— Projected magnetic energy density of runs A to F at different redshifts. Each image is 8 Mpc on a side and centered at the cluster center. The projected results are obtained by integrating 8.0 Mpc centered at the cluster center along lines perpendicular to the observed plane. The color range is from 1.0×10^8 (blue) to 1.0×10^{12} (red) ergs cm $^{-2}$.

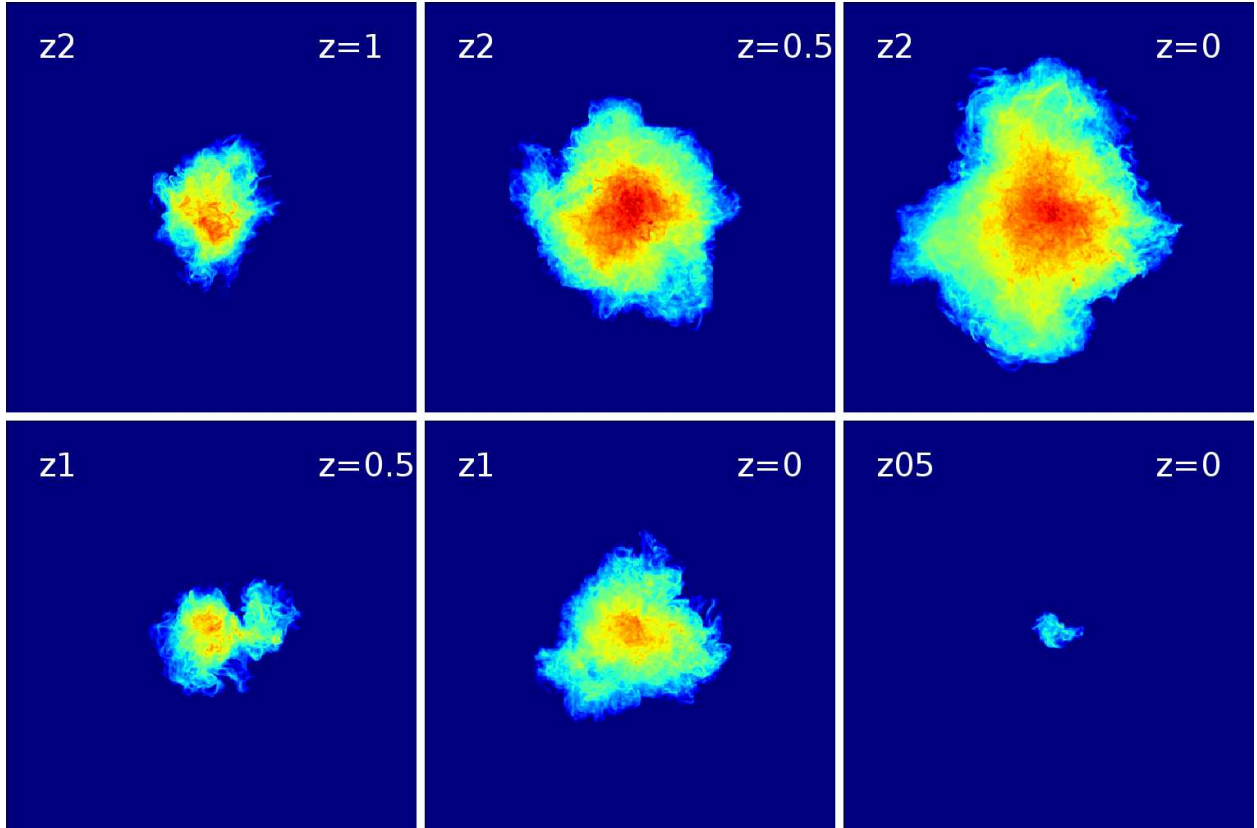


Fig. 6.— Similar to Fig. 5, except for runs z2, z1 and z05.

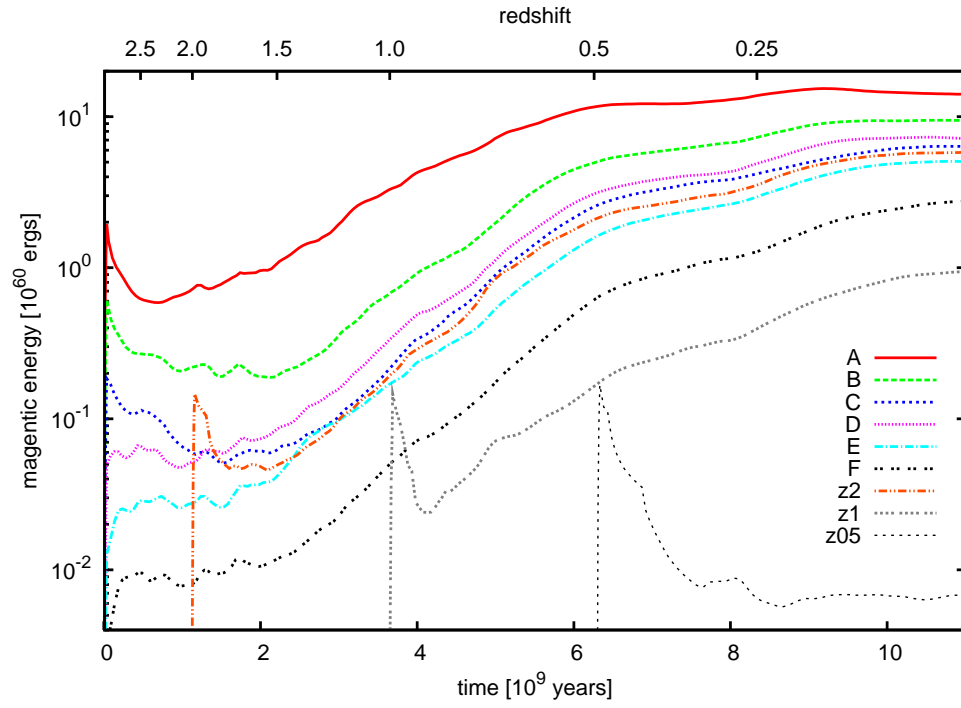


Fig. 7.— Evolution of total magnetic energy of all simulations.

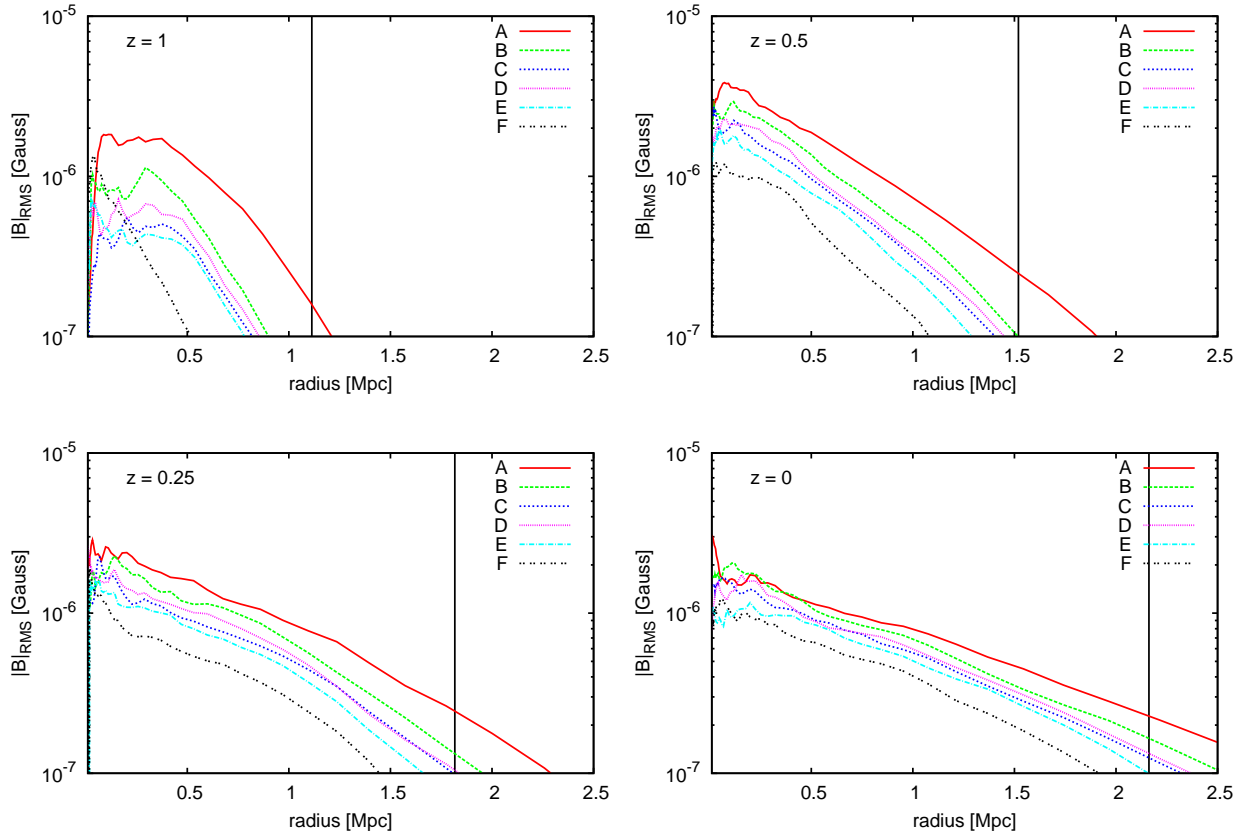


Fig. 8.— The spherically averaged radial profile of RMS magnetic field strength at different epochs of the cluster formation. The radius is measured in the proper distance Virial radii are marked by vertical lines.

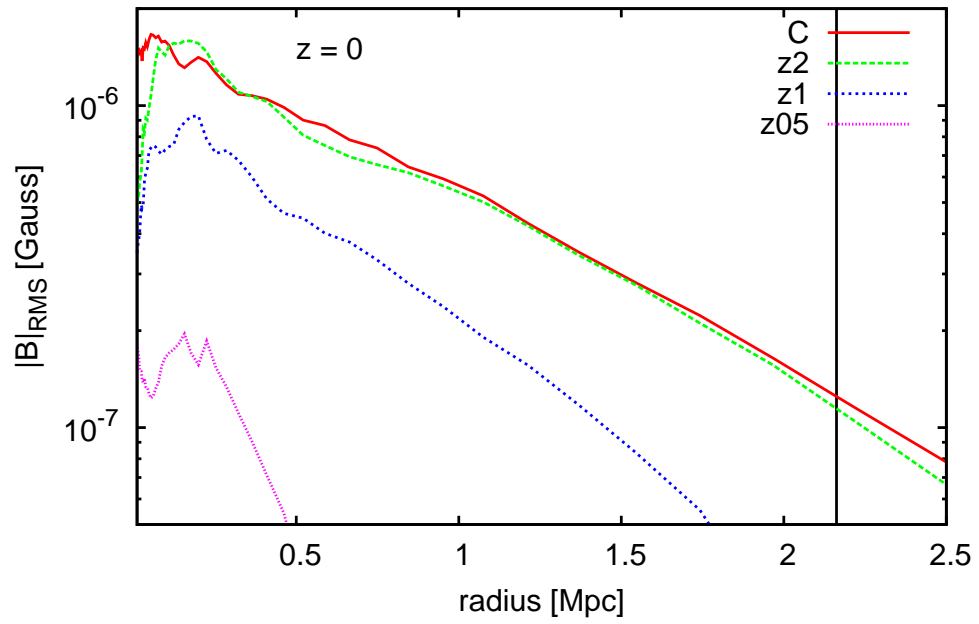


Fig. 9.— The spherically averaged radial profile of RMS magnetic field strength at $z=0$ of runs C, z2, z1, z05.

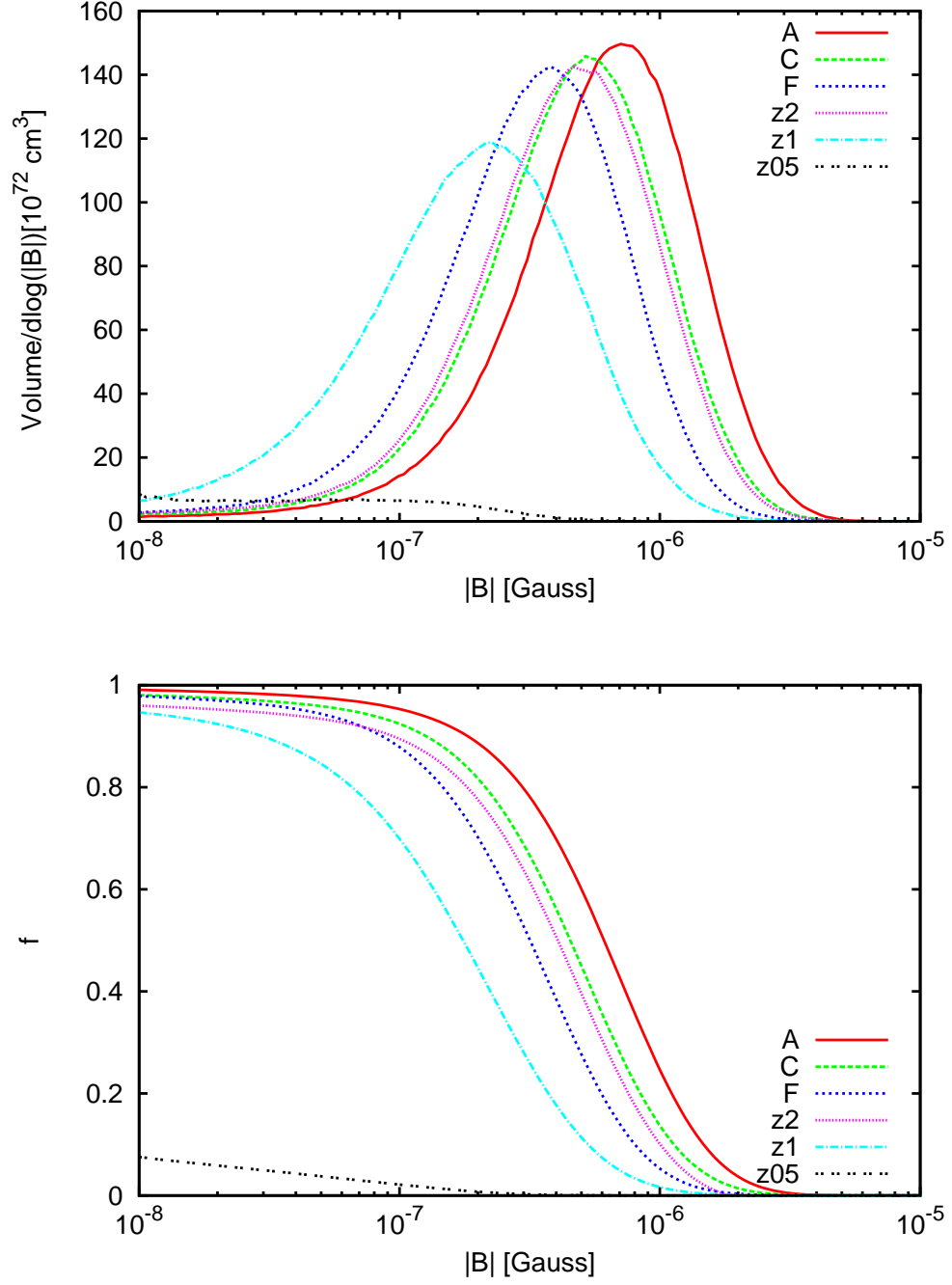


Fig. 10.— Volume histogram (Top) and complementary cumulative volume histogram ($f(B) = \int_B^\infty P(B')dB'$) (Bottom) of magnetic field strength of the central 1 Mpc sphere at $z = 0$.

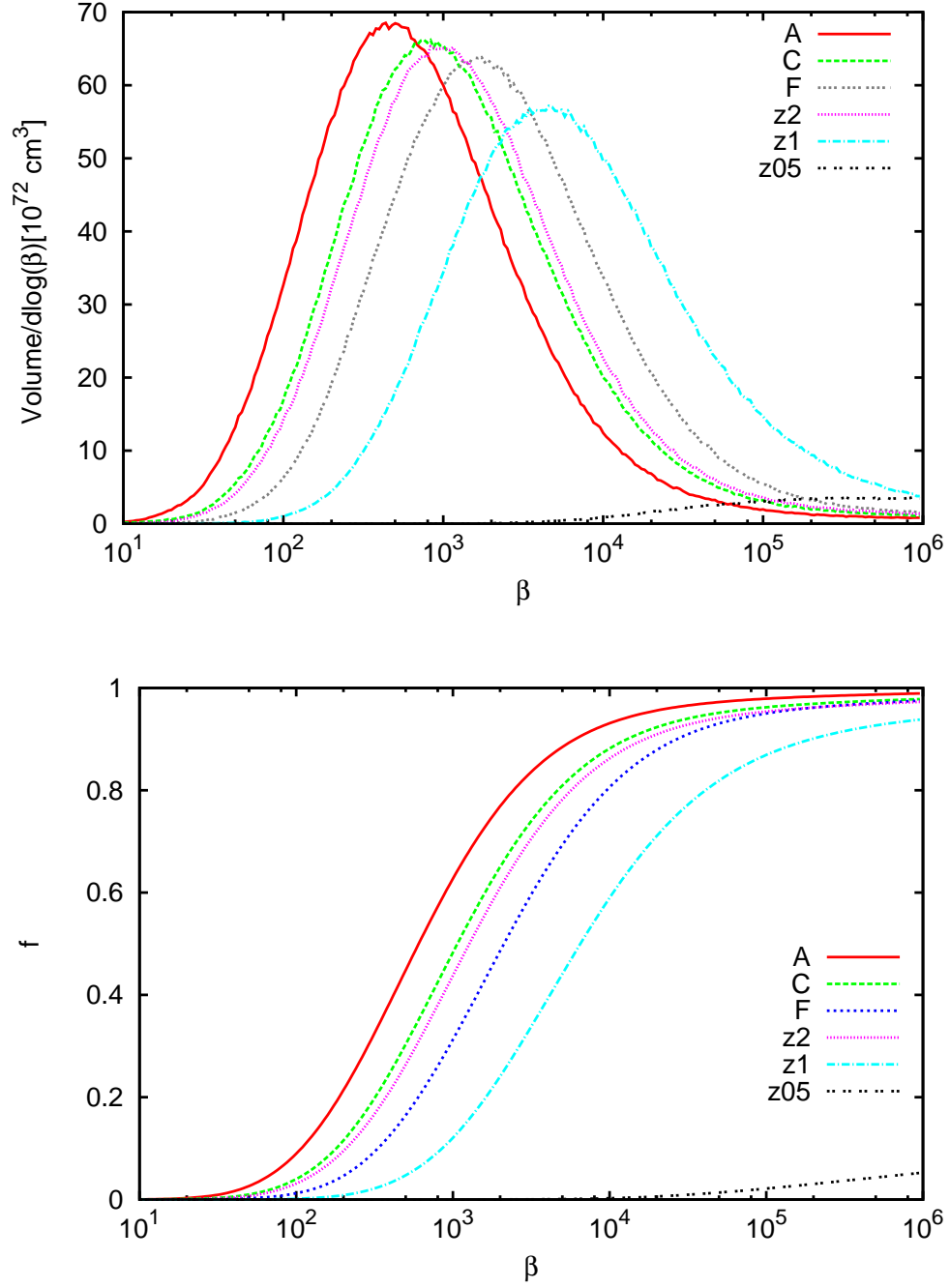


Fig. 11.— Volume histogram (Top) and cumulative volume histogram (Bottom) of plasma β of the central 1 Mpc sphere at $z = 0$.

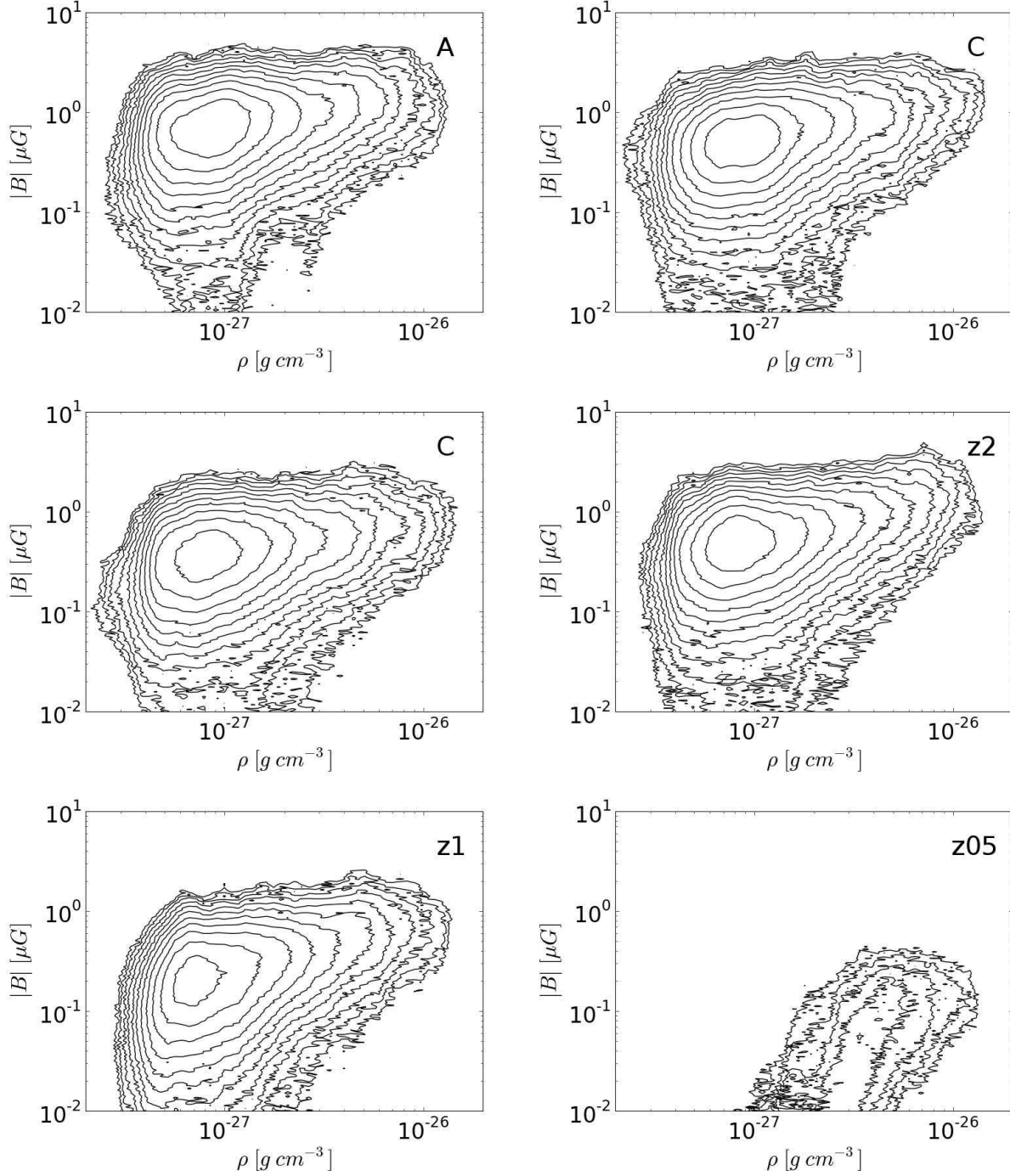


Fig. 12.— Volume weighted two-dimensional distributions of the magnetic field strength vs. baryon density of runs A, C, F, z2, z1, z05 inside the cluster core of 1 Mpc sphere at $z = 0$. Contour lines are the volume of gas at that density and magnetic field at 10^k cm³, where k = 69.0, 69.2, 69.4, ... 71.2 from outer to inner.

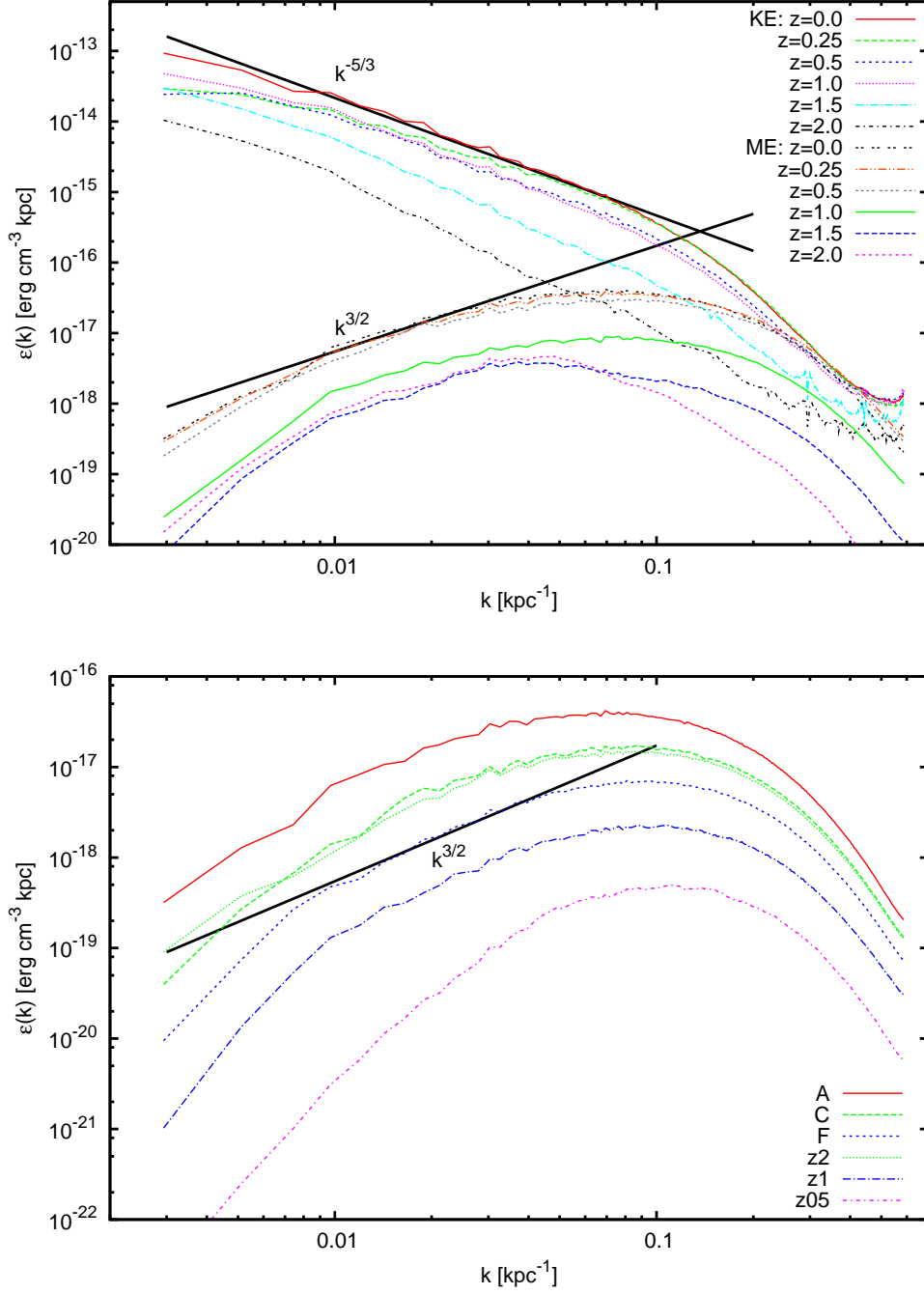


Fig. 13.— Top panel: Power spectra of the kinetic energy density and magnetic energy density of the ICM of run A at different redshifts. The ICM turbulence is represented by the Kolmogorov-like spectra in kinetic energy. The magnetic energy spectra follow the $k^{3/2}$ Kazantsev law in large scale. Bottom panel: Magnetic energy spectra of runs A, C, F, z2, z1, z05. All spectra except run z05 show a short $k^{3/2}$ range.

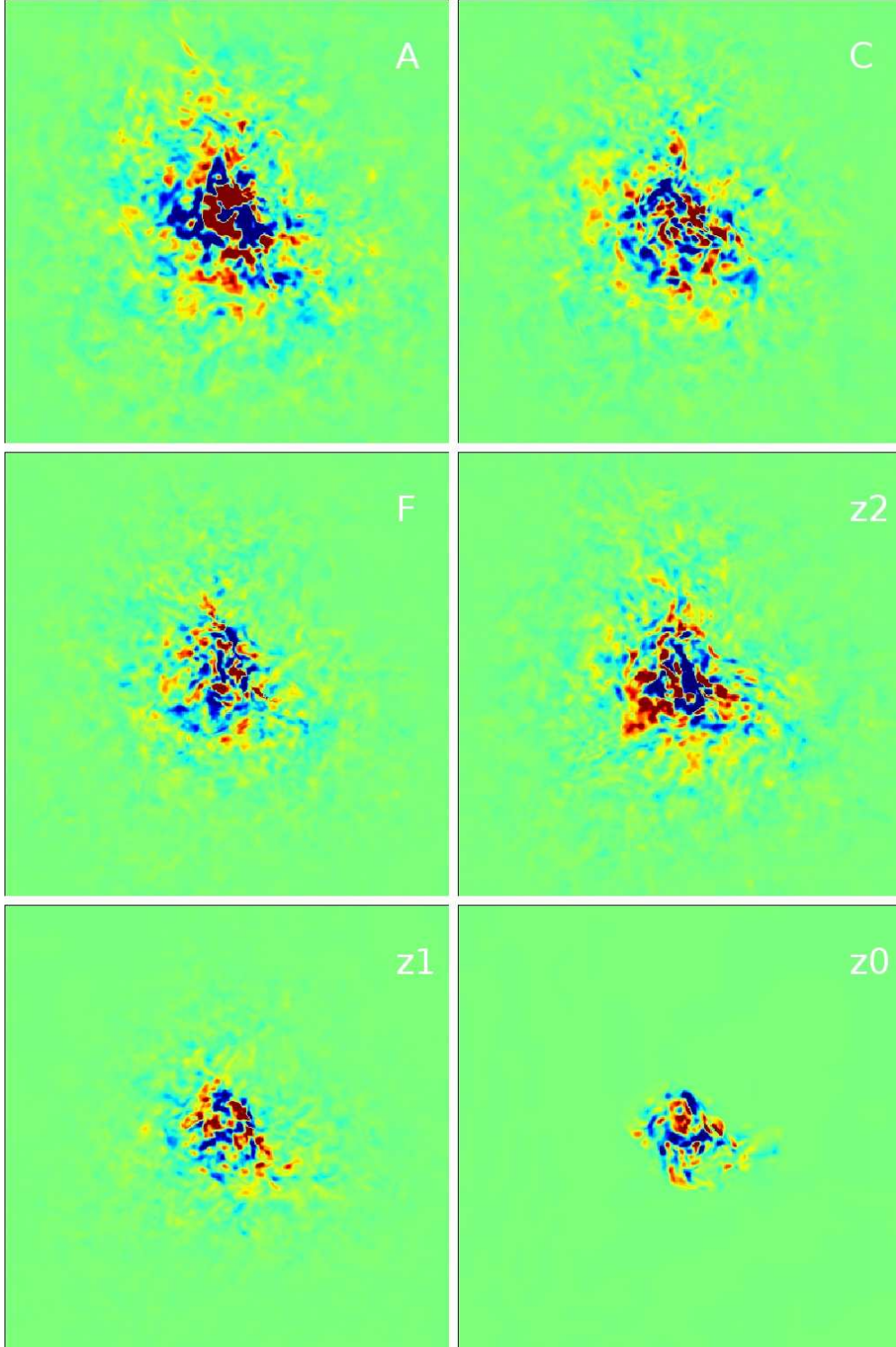


Fig. 14.— Faraday rotation measurement of the ICM by integrating through the cluster along the y direction for different runs. It covers a region of $3 \text{ Mpc} \times 3 \text{ Mpc}$ at $z = 0$. The color range shown is from -500 (blue) to 500 (red) rad m^{-2} .

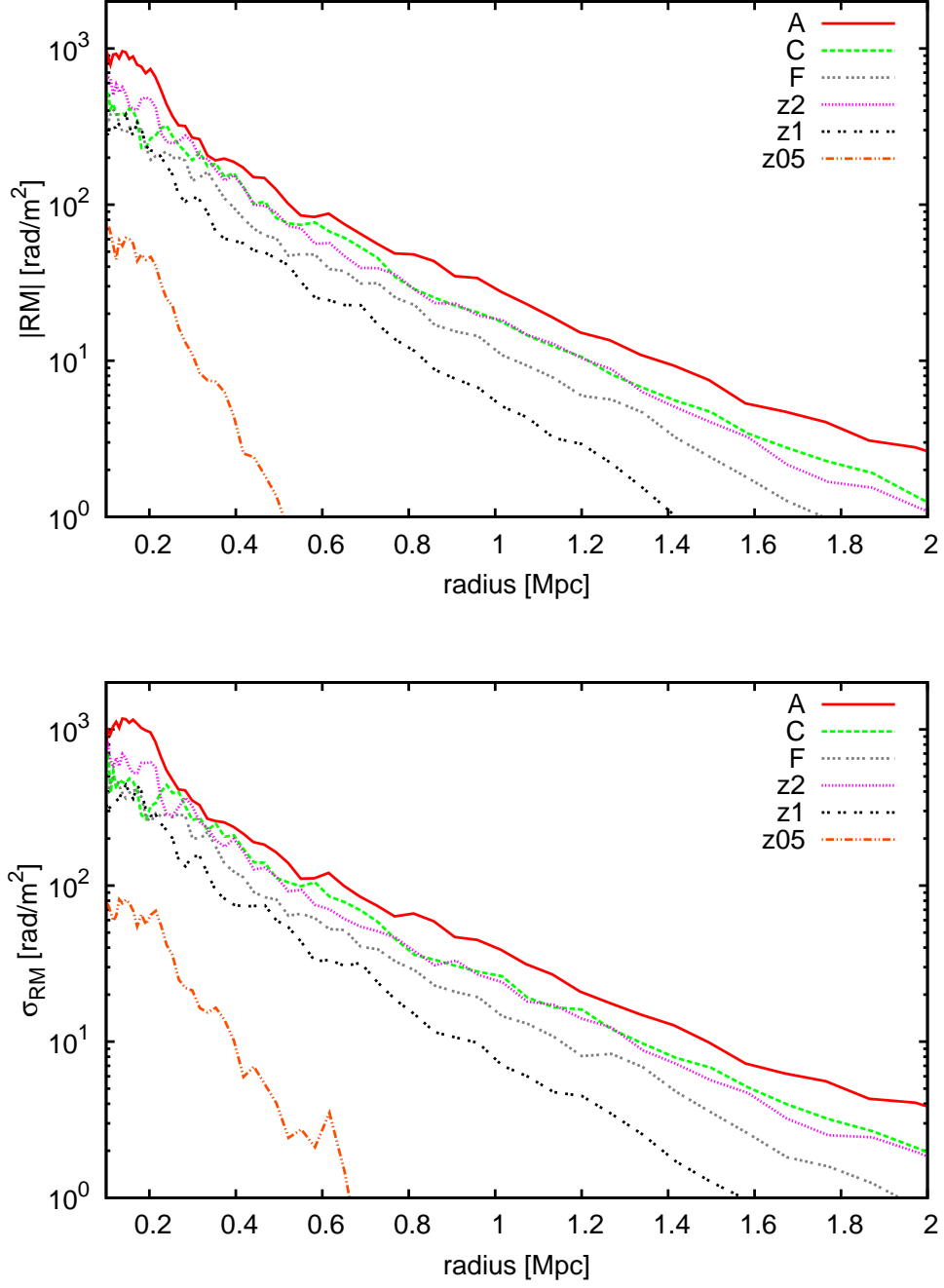


Fig. 15.— The circularly averaged radial profiles of $|RM|$ observed from y direction at $z = 0$ (top) and the radial profiles of the standard deviation (σ_{RM}) of the same RM distribution (bottom).

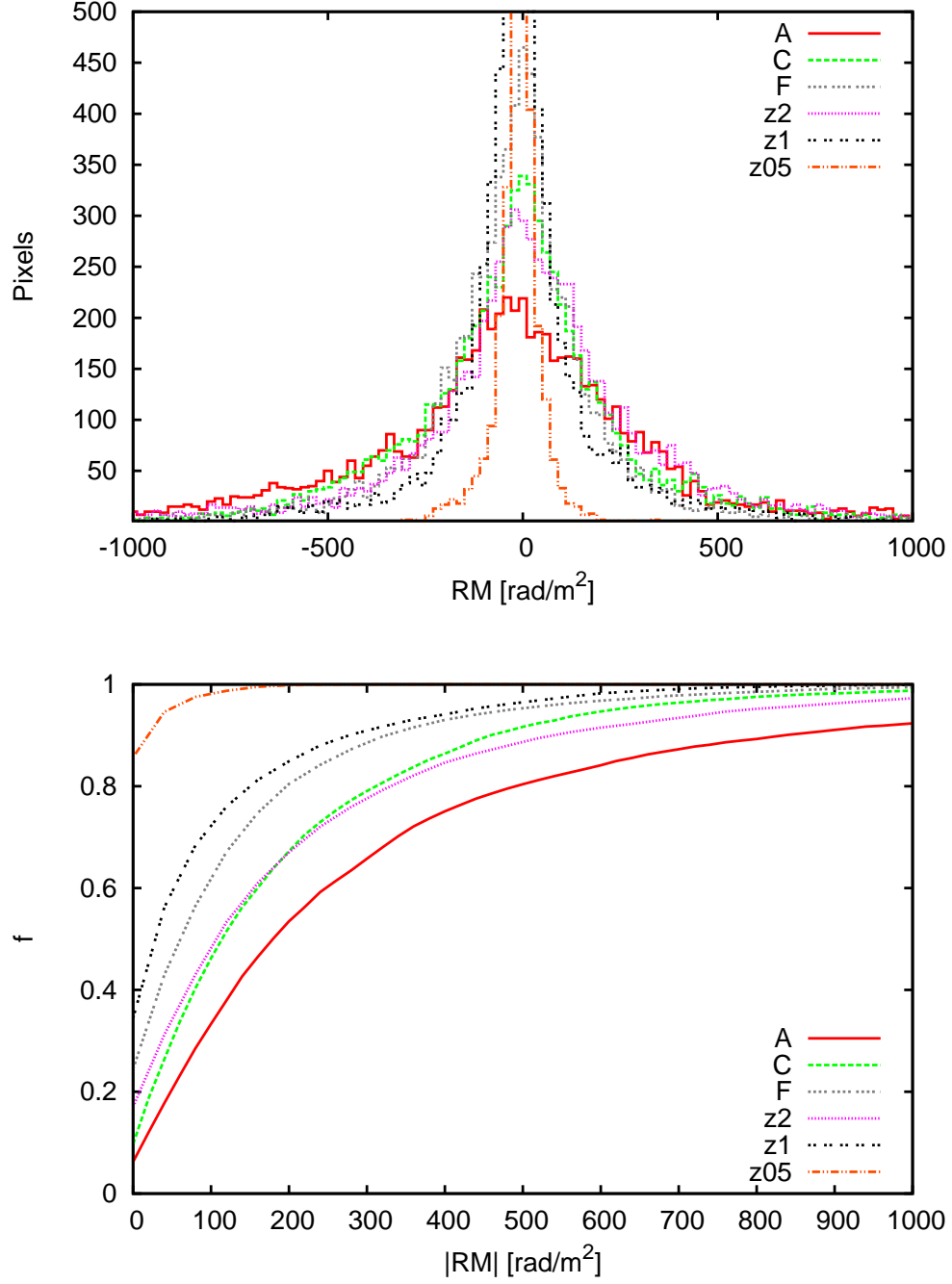


Fig. 16.— Area histogram (top) and cumulative area histogram (bottom) of RM observed from the y direction of the central circle of 0.5 Mpc radius at $z = 0$. Each pixel represents $7.81 \text{ h}^{-1} \text{ kpc} \times 7.81 \text{ h}^{-1} \text{ kpc}$.

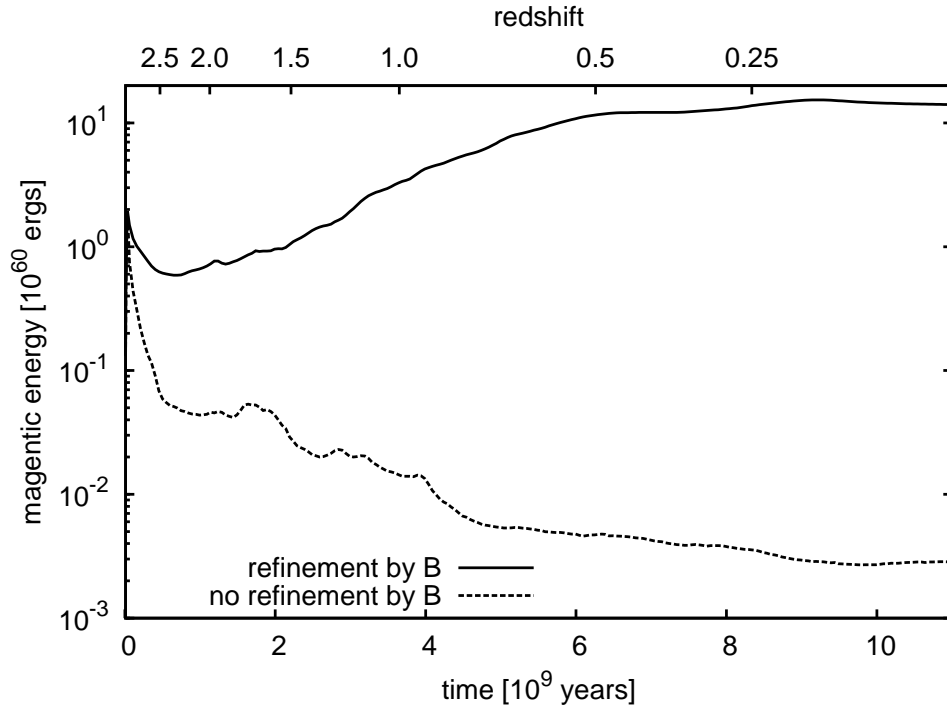


Fig. 17.— Magnetic energy evolution of the injection run A with and without refinement by the magnetic field strength.

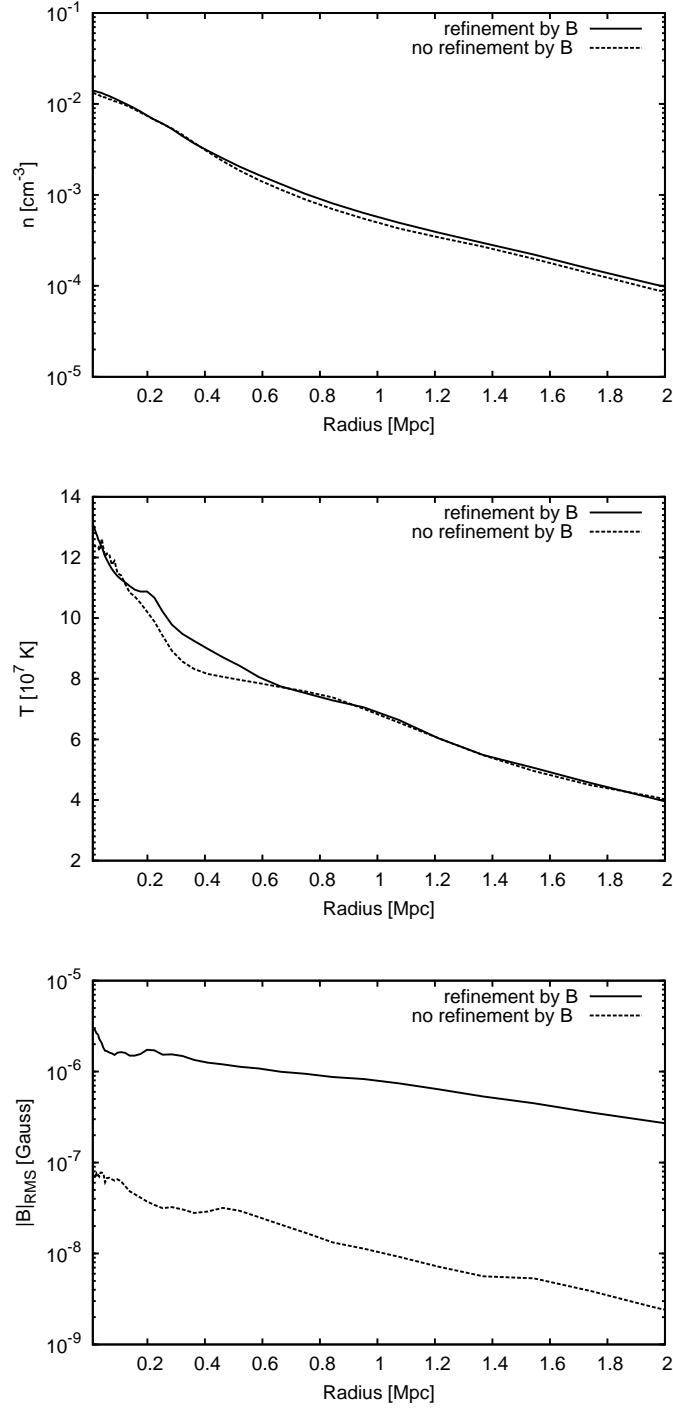


Fig. 18.— Spherically averaged radial profiles of baryon density (top), temperature (middle) and RMS magnetic field strength (bottom) at $z = 0$ for cases with and without refinement by the magnetic field strength.